Vacancy pair induced surface chemistry reconstruction of $Cs_2AgBiBr_6$/Bi_2WO_6 heterojunction to enhance photocatalytic CO_2 reduction

Hao Wang [a,c], Xilun Wang [a], Peng Hu [a,b], Ting Liu [c], Bo Weng [d], Kai-hang Ye [e], Yongming Luo [c,*], Hongbing Ji [a,b,**]

[a] School of Chemistry, Sun Yat-sen University, Guangzhou, Guangdong 510275, PR China
[b] State Key Laboratory Breeding Base of Green Chemistry-Synthesis Technology, Institute of Green Petroleum Processing and Light Hydrocarbon Conversion, College of Chemical Engineering, Zhejiang University of Technology, Hangzhou 310014, PR China
[c] Faculty of Chemical Engineering, Kunming University of Science and Technology, Kunming, Yunnan 650500, PR China
[d] cMACS, Department of Microbial and Molecular Systems, KU Leuven, Celestijnenlaan 200F, Leuven 3001, Belgium
[e] Institute for Sustainable Transformation, School of Chemical Engineering and Light Industry, Guangdong University of Technology, Guangzhou, Guangdong 510006, PR China

ARTICLE INFO

ABSTRACT

$Cs_2AgBiBr_6$/Bi-O vacancy pair Bi_2WO_6 ($Cs_2AgBiBr_6$/$V_{Bi-O}Bi_2WO_6$) heterojunction was synthesised for photocatalytic CO_2 reduction under visible light irradiation. The characterisation results show that the Bi-O vacancy pairs can reconstruct the surface electronic states of the heterojunction. The optimal 10%$Cs_2AgBiBr_6$/$V_{Bi-O}Bi_2WO_6$ heterojunction exhibited a substantial CO yield of 48.5 μmol/g, approximately 22 times higher than that of Bi_2WO_6, exceeding the performance of most of the Bi-based photocatalysts reported to date. The enhanced activity of 10%$Cs_2AgBiBr_6$/$V_{Bi-O}Bi_2WO_6$ was due to exposed Bi sites that facilitate the chemisorption and activation of CO_2 and the lower reaction energy barrier for the protonation of CO_2 to CO via the formation of COOH* intermediates with the cooperation of surface four-coordinated H_2O molecules. Furthermore, charge migration from $Cs_2AgBiBr_6$ to $V_{Bi-O}Bi_2WO_6$ and space-charge distribution in the heterojunction under visible light irradiation were demonstrated. This work reveals defective heterojunction catalysts that facilitate the transformation of reactive molecules in surface/interfacial reactions.

1. Introduction

The use of semiconductor photocatalysts to convert CO_2 greenhouse gas into high-value-added fuels provides an ideal way to solve the current environmental and energy problems. However, the high chemical stability of CO_2 is accompanied by a high C=O dissociation energy of 750 kJ/mol [1–3]. Therefore, photocatalytic CO_2 reduction, which involves complex multi-electron transfer kinetic processes and surface interfacial CO_2 molecular catalytic activation processes, is usually difficult to achieve. After decades of research, photocatalysts with high quantum efficiencies for CO_2 reduction are being achieved [4,5]. Current research mainly focuses on modifying photocatalytic materials by elemental doping, regulating the nanomorphology and crystal surface structure, and loading nano-cocatalysts [6–8]. Specifically, TiO_2 with different morphologies or doped with elements such as N and Pd, along

with co-catalysts such as CeO_2 and $CuInS_2$, have been shown to effectively increase the light capture efficiency and the separation and conversion rates of electron holes [9–12]. The catalytic reactions mainly occur at the active sites on the catalyst surface. Therefore, the effective design of catalysts for photocatalytic CO_2 reduction based on a comprehensive consideration of the semiconductor band structure and surface reaction process is extremely challenging.

Bi_2WO_6 two-dimensional nanosheets are Aurivillius oxides, and the well-organised crystal arrangement and strong bonds between adjacent $(Bi_2O_2)^{2+}$ and $(MoO_4)^{2-}$ layers result in excellent photoelectric properties and visible light response [13–15]. Furthermore, Bi_2WO_6 is easy to synthesise. Despite these advantages, the perfect crystalline phase structure of pure Bi_2WO_6 has some limitations for CO_2 reduction, such as insufficient redox potential, inevitable carrier recombination, limited CO_2 adsorption capacity, and difficult surface hybridization [16]. To

---

* Corresponding author.
** Corresponding author at: School of Chemistry, Sun Yat-sen University, Guangzhou, Guangdong 510275, PR China.
E-mail addresses: environcatalysis@kust.edu.cn (Y. Luo), jihb@mail.sysu.edu.cn (H. Ji).

address these limitations, surface defect engineering is considered one of the most effective strategies for increasing the reaction rate and efficiency of charge migration, and enhancing the activation of surface reaction molecules. Researchers have mainly focused on introducing individual anion defects into the two-dimensional Bi_2WO_6 surface to improve its physical properties and photocatalytic activity [17,18]. When the thickness of Bi_2WO_6 is reduced to the molecular level, the atoms in the $[Bi_2O_2]^{2+}$ and $[WO_4]^{2-}$ layers escape from the surface to form defects due to the small atomic escape energies. However, vacancy pairs in Bi_2WO_6 have rarely been reported because it is very difficult to design and manipulate vacancy pairs using a stable and reliable method [19].

In addition, strain-induced high-energy surface structures generated by vacancy pairs can regulate the electronic structure of local atoms and reconstruct the surface electronic states [20–23]. The open metal sites and ligand unsaturated sites can act as gaps on the surface of the heterojunction, thereby optimising the electron transport pathways and enriching surface-active centres, thereby significantly altering the catalytic behaviour. However, the preparation of heterojunction catalysts using Bi_2WO_6 nanosheets containing vacancy pairs is complex. There are still bottlenecks and difficulties in exploring and developing safe, stable, and inexpensive co-catalysts for the in situ synthesis of heterojunction catalysts using Bi_2WO_6 nanosheets containing vacancy pairs. Since $Cs_2AgBiBr_6$ was first reported as an active layer in 2017, it has been widely evaluated as a representative lead-free halogenated double perovskite co-catalyst for photocatalysis [24,25]. The rational design of $Cs_2AgBiBr_6$/semiconductor heterojunctions has shown great potential for enhancing their photocatalytic performance for CO_2 reduction. Xu et al. reported the synthesis of $Cs_2AgBiBr_6/C_3N_4$ heterojunctions for CO_2 reduction to CO; the CO yield of $Cs_2AgBiBr_6/C_3N_4$ was 10 times higher than that of pure C_3N_4 [26]. Similarly, $Cs_2AgBiBr_6$/GO hybrid materials were successfully fabricated for photocatalytic activity [27]. The similar Bi atomic density of states and electron binding energies of the $Cs_2AgBiBr_6$ and Bi_2WO_6 crystals resulted in excellent interfacial matching between them, which enabled the efficient migration and separation of photogenerated electron–hole pairs. A comprehensive and in-depth exploration of the effects of the structure and surface properties of defective $Cs_2AgBiBr_6/Bi_2WO_6$ catalysts on photocatalytic CO_2 reduction is challenging.

Herein, inspired by this analysis, we report the synthesis of $Cs_2AgBiBr_6$ quantum dots/Bi–O vacancy pair Bi_2WO_6 heterojunctions (CABB/$V_{Bi–O}$BWO) with enhanced surface reaction kinetics for effective photocatalytic CO_2 reduction under visible light irradiation. The presence of surface Bi-O vacancy pairs can induce the reconstruction of surface states in $V_{Bi–O}$BWO, whereas the vacancies can act as an interface to confine the surface $Cs_2AgBiBr_6$ quantum dots to form a tight CABB/$V_{Bi–O}$BWO heterojunction, as demonstrated by the X-ray absorption spectroscopy and positron annihilation results. The optimised 10CABB/$V_{Bi–O}$BWO heterojunction exhibited superior photocatalytic activities for CO, CH_4, and O_2 production, which were 22, 9, and 20 times higher than those of pure Bi_2WO_6, respectively. The enhanced photocatalytic activity was attributed to the enhanced adsorption, favourable activation, and low reaction free-energy path of CO_2 molecules on the CABB/$V_{Bi–O}$BWO surface in the simulated catalytic reduction processes. The molecular coordination structures and key intermediate species on the catalyst surface were detected using in situ molecular spectroscopy to evaluate the photocatalytic CO_2 reduction reaction pathway. In situ irradiation X-ray photoelectron spectroscopy, femtosecond time-resolved spectroscopy, and Kelvin probe force microscopy confirmed the authenticity of the photogenerated charge transfer pathway and the charge transfer efficiency of the CABB/$V_{Bi–O}$BWO samples for photocatalytic CO_2 reduction. Finally, a mechanism for the surface catalytic effect that promotes the photocatalytic CO_2 conversion of the CABB/$V_{Bi–O}$BWO nanosheets was proposed.

2. Experimental section

2.1. Preparation of layered Bi_2WO_6 compounds

First, 1.94 g of $Bi(NO_3)_3 \cdot 5 H_2O$ and 0.66 g of $Na_2WO_4 \cdot 2 H_2O$ were added to 80 mL of deionised water and stirred vigorously for 1 h to achieve even dispersion. Then, the mixture was transferred to a 100 mL polytetrafluorethylene (PTFE)-lined autoclave, sealed and heated at 120°C for 24 h. After the autoclave was naturally cooled to room temperature, the white precipitate was washed several times with ethanol and deionised water to remove surface contaminants. The final Bi_2WO_6 powder product was obtained by drying at 60 °C for 12 h and labeled as BWO [28].

2.2. Synthesis of $V_{Bi-O}Bi_2WO_6$ nanosheets

First, 0.49 g of $Bi(NO_3)_3 \cdot 5 H_2O$ was dissolved in 45 mL of 0.1 mol/L mannitol solution under continuous stirring. Then, 0.4 g of PVP was then added to the solution under continuous stirring. After stirring for 1 h, 10 mL of KBr solution (0.1 mol/L) was rapidly injected into the above mixture and stirred for 1 h. Subsequently, the mixture was transferred to a 100 mL PTFE-lined autoclave and maintained at 160 ℃ for 3 h. After naturally cooling to 30 ℃, the prepared samples were obtained by centrifugation and washed several times with deionised water and ethanol. The final BiOBr powder product was obtained by drying at 60 °C for 12 h. Subsequently, 0.15 g of the synthesized BiOBr samples were dispersed in 40 mL H_2O, and 0.33 g $Na_2WO_4 \cdot 2 H_2O$ was added to the dispersion solution and stirred at 25℃ for 1 h. Then, the mixture was transferred to a 100 mL polytetrafluorethylene (PTFE)-lined autoclave, sealed and heated at 140°C for 1 h. After naturally cooling to 30 ℃, the prepared samples were obtained by centrifugation and washed several times with deionised water and ethanol. The final defective Bi_2WO_6 powder product was obtained by drying at 60 °C for 12 h and labeled as V_{Bi-O}BWO.

2.3. Fabrication of $Cs_2AgBiBr_6$ quantum dots

First, a Cs-oleate solution was prepared by adding Cs_2CO_3 (0.814 g) to a mixture of octadecene (40 mL) and oleic acid (2.5 mL) in a three-necked flask and stirring continuously for 1 h. Subsequently, the mixture was heated to 150 °C in a N_2 atmosphere and maintained for 1 h to form the Cs-oleate solution. This solution was maintained at 120 °C for subsequent use.

To synthesise the $Cs_2AgBiBr_6$ quantum dots, 450 mg of $BiBr_3$,170 mg of $AgNO_3$, 20 mL of ODE, 0.5 mL of HBr, 5 mL of OA, and 5 mL of OLA were mixed in a 100 mL three-neck flask, degassed, and heated to 120 ℃ for 1 h under continuous stirring to remove excess gas. The mixture was then heated to 200 ℃ at a rate of 5°/min under nitrogen. Then, 8 mL of the previously prepared Cs-oleate solution (120 ℃) was rapidly injected into the mixture under continuous agitation. After 30 s, the mixture was rapidly cooled to 0 ℃ by transferring the three-necked flask to an ice water bath. The obtained yellow precipitate was washed with chloroform by repeated centrifugation and dried under vacuum at 60 ℃ to obtain the $Cs_2AgBiBr_6$ quantum dots (denoted as CABB).

2.4. Synthesis of $Cs_2AgBiBr_6/V_{Bi-O}Bi_2WO_6$

A certain amount of CABB powder and 100 mg of V_{Bi-O}BWO powder were mixed in 10 mL of carbon tetrachloride solution, and the mixture was ultrasonically dispersed for 3 min, followed by continuous stirring for 1 h in the dark. Finally, the $Cs_2AgBiBr_6/V_{Bi-O}Bi_2WO_6$ complex was obtained by centrifugation at 8000 rpm for 5 min and vacuum drying at 60 ℃ for 1 h. The weight percentages of CABB relative to $V_{Bi-O}Bi_2WO_6$ were set to 5%, 7.5%, 10%, and 12.5%, and the corresponding samples were labelled 5CABB/V_{Bi-O}BWO, 7.5CABB/V_{Bi-O}BWO, 10CABB/V_{Bi-O}BWO and 12.5CABB/V_{Bi-O}BWO, respectively.

2.5. General characterisation

The zeta potentials of the samples were measured using a Zetasizer (Nano ZS90, Malvern Instruments, Ltd.). Powder X-ray diffraction (PXRD) patterns of the samples were recorded using a Bruker D8 Advance instrument with a Cu K_{α} source over a scanning range of 20–60° at 40 kV and 40 mA. The morphology and crystallinity of the samples were examined using spherical aberration-corrected scanning transmission electron microscopy (STEM, JEM-ARM200P), and EDS analysis (Bruker Xflash 5030 T) operated at an accelerating voltage of 200 kV. Initially, 5 mg of the sample was dispersed in 10 mL of methanol using ultrasound for 3 min. Subsequently, a pipette gun was utilized to extract 10 microliters of the dispersion and deposit it onto the holder for testing. The size and thickness of the samples were measured using atomic force microscopy (AFM; Agilent 5500 AFM, Agilent Technologies, USA). Similarly, 5 mg of the sample was dispersed in 10 mL of methanol using ultrasound for 3 min. Subsequently, a pipette gun was utilized to extract 10 microliters of the dispersion and deposit it onto the holder for testing. Kelvin probe force microscopy (KPFM) was performed under ambient conditions using a Bruker Dimension Fastscan. UV−vis diffuse reflectance spectroscopy (UV−vis DRS, UV2450 spectrophotometer, Cary 5000 Varian, USA) was performed to investigate the photoabsorption properties of the samples, using $BaSO_4$ as a reference. The 30 mg sample was placed in the sample cell and calibrated with $BaSO_4$ prior to testing. The CO_2 adsorption curves of the samples were obtained using a fully automated physicochemical adsorption analyser (Micromeritics ASAP 2460, USA) at 25℃. Raman spectroscopy was performed using a Nicolet NXR 9650 over the wavenumber range from 50 to 1000 cm^{-1}. XPS of the samples was performed using an Escalab 250 instrument (Thermo Fisher, UK) with a monochromatic Al K_{α} radiation source, with the binding energy of the C1s peak located at 284.8 eV taken as the reference. UPS measurements of the samples were also performed using an Escalab 250 instrument with a He I source (21.22 eV) at a bias of −10.0 V. Electron paramagnetic resonance (EPR) measurements were performed at 25°C using a JAS-FA200 spectrometer.

2.6. In situ Raman spectroscopy

In situ Raman spectra of water adsorbed on the samples were collected using a confocal microscope Raman system (Renishaw Invia) at a resolution of 4 cm^{-1} using 64 scans per spectrum. A 632 nm laser and a 50× microscope objective were used for all samples. First, the tested samples were prepared as discs (10 mg, 10 mm diameter), which were then transferred onto an in situ reaction chamber and placed under the objective lens of the Raman system. Before testing, the Raman frequency was calibrated using a Si wafer. The Raman spectra of all samples were collected under dark conditions. Subsequently, water vapor was injected onto the sample surface by a bubbling method. After adsorption equilibration, the interaction between the sample and water was characterised by Raman spectroscopy under irradiation.

2.7. In situ irradiated X-ray photoelectron spectroscopy (In situ XPS)

In situ irradiated XPS measurements were performed using an Escalab 250 instrument, as previously reported by our group. The charge migration path was determined by exploring the variation in electron cloud density of sample before and after irradiation. First, a 5 mg sample was prepared as a disc with a diameter of 5 mm. The disc was then placed on a sample holder that could be moved horizontally using a manipulator. Before being transferred to the analysis chamber for in situ XPS measurements, the samples were pretreated under dynamic vacuum (8×10^{-9} Torr) for 12 h to remove surface contaminants. Considering that the sample exhibited a significant visible light response, as confirmed by DRS. Therefore, a 405 nm laser was introduced into the XPS chamber. Subsequently, the sample was transferred to the analysis chamber and placed 2 cm away from the laser by a manipulator. The sample was initially analyzed under dark conditions. Subsequently, to achieve a balanced separation of electrons and holes, the sample was illuminated for 2 min for subsequent testing. Ultimately, the shift of the XPS peaks associated with the elements in the sample was employed to investigate charge migration both before and after light irradiation.

2.8. In situ diffuse reflectance infrared fourier transform spectroscopy (In Situ DRIFTS)

In situ DRIFTS spectra were obtained in the wavenumber range of 1800–1100 cm^{-1} using a Nicolet iS20 instrument (ThermoFisher Corp., USA) equipped with an in situ diffuse cell, a light source, and a Hg–Cd–Te detector cooled by liquid nitrogen. The in situ reaction chamber was equipped with ZnSe windows and an inlet and outlet for introducing gas. Before testing, 100 mg of catalyst was added to the in situ reaction cell and then pretreated at 180 ℃ for 1 h under a nitrogen atmosphere to remove impurities. The background spectra of all samples were recorded in an Ar atmosphere and then subtracted from the sample spectra. CO_2 and Ar gases (V_{CO2}:V_{Ar}=1:3) were introduced into the inlet of the in situ chamber at 8 mL/min via a mixing tank with water. The in situ DRIFTS spectra of the samples were recorded at 0 min in Ar atmospheres under light irradiation. Subsequently, CO_2 and water vapour were continuously injected into the in situ reaction chamber and the spectra were collected over time under continuous irradiation. The temperature of the in situ reaction cell was maintained at 25 ℃ by circulating cooling water.

2.9. Synchrotron-radiation X-ray absorption fine structure (XAFS) spectroscopy

XAFS of the samples was performed on a 21 A X-ray nanodiffraction beam at the Taiwan Photon Source, National Synchrotron Radiation Research Center. This beamline uses a 4-bounce channel-cut Si (111) monochromator for monobeam XAFS. The end station was equipped with three ionisation chambers and a Lytle/SDD detector after the focusing position of a Kirkpatrick–Baez mirror for transmission- and fluorescence-mode XAFS. The photon flux on the sample was in the range of 1×10^{11} – 3×10^9 photon/s for an X-ray energy of 6–27 keV.

2.10. Density functional theory (DFT) calculations

The CO_2 reduction process of the catalysts was investigated using the Vienna Ab-Initio Simulation Package (VASP). The projector augmented-wave pseudopotential method was used to describe the electron–ion interactions. We used the Perdew–Burke–Ernzerhof generalised gradient approximation to treat the exchange and correlation functionals. The cutoff energy for the wave function expansion was set to 450 eV, the self-consistent total-energy difference was set to 1.0×10^{-5} eV, and the convergence criterion for forces on atoms was set to 0.025 eV/Å. A K-point grid of $4 \times 4 \times 1$ was set as the Brillouin zone to achieve geometric optimisation and improve the simulation accuracy. The BWO, V_{Bi-O}BWO and 10CABB/V_{Bi-O}BWO models were constructed based on their corresponding crystal structures using DFT calculations. The slab models were set as a vacuum layer with a thickness of 15 Å in the z direction for all configurations to avoid the interaction between the adsorbate and periodic images. The free energy was calculated as follows: $\Delta G = \Delta E + \Delta ZPE - T\Delta S$, where ΔE is the total energy for the calculated geometric configuration, ΔZPE is the zero-point energy, and ΔS is the reaction entropy change correction.

2.11. Photoelectrochemical measurements

Photoelectrochemical measurements were performed using an electrochemical workstation (CHI660C, Chenhua Instruments, Shanghai, China) equipped with a three-electrode cell. A saturated calomel

electrode was used as the reference electrode, a platinum plate was used as the counter electrode, and the catalyst was smeared on fluorine-doped tin oxide conducting glass to form a thin film for use as the working electrode. Anodic photocurrent response measurements were performed in 0.5 mol/L Na_2SO_4 solution with a 300 W Xe light source ($\lambda \geq 420$ nm). LSV tests were performed in 0.2 mol/L Na_2SO_4 solution at a scan rate of 5 mV/s. CV measurements were performed in 0.5 mol/L Na_2SO_4 solution containing 0.01 M $K_3[Fe (CN)_6]/K_4[Fe (CN)_6]$ (1 : 1) at a scan rate of 50 mV/s.

2.12. Evaluation of photocatalytic CO_2 reduction performance

Photocatalytic CO_2 reduction measurements were performed using a Labsolar-6A all-glass automatic online trace-gas analysis system (Beijing Perfectlight) in the presence of H_2O. Considering the fact that water serves as an exceptional hydrogen source donor, acetonitrile exhibits enhanced CO_2 solubility, thereby ensuring the initial step in achieving efficient photocatalytic conversion of CO_2. Initially, 30 mg of the catalyst was dispersed in a mixture of 50 mL of deionised water and 50 μL of acetonitrile with constant agitation. A glass cover was then placed on top of the reactor. The reaction system was pumped to achieve sufficient vacuum, followed by introducing high-purity CO_2 via a flowmeter. The CO_2 purging process was repeated three times to eliminate as much air from the reaction system as possible. Pure CO_2 gas was subsequently introduced into the closed system to achieve a pressure value of 80 Kpa, enough to firmly press against the glass cover of the reactor, ensuring the air-tightness of the reaction system. The pressure in the reactor is typically controlled slightly below atmospheric pressure. The temperature of the reactor was maintained at 25 ℃ by injecting condensate circulating water into the outer wall of the reactor. The resulting gas products were quantitatively analysed using gas chromatography with a thermal conductivity detector and a hydrogen flame ionisation detector at one-hour intervals using an automated injection method. 5 A molecular sieve column was applied for separation of product. The carrier gas used was argon with a purity of 99.999%, flowing at a constant rate of 20 mL min^{-1}. The temperatures for the injector and detector were set at 120 °C and 180 °C, respectively. The initial column temperature was set at 70 °C. The product yield was calculated by integrating the peak using the external standard method. A 300 W xenon lamp (PLS-SXE300D, Beijing Perfectlight) with a 420 nm filter with a light intensity of 150 mW/cm^2 was utilized as the reaction light source.

2.13. Apparent quantum yield measurements

The apparent quantum yield (AQY) of the sample was performed using a 300 W xenon lamp equipped with 400, 420, and 470 nm band-pass filters, while other conditions remained unchanged. A PL-MW2000 optical power meter was used to measure the photon flux of the incident light. Based on the CO generated during the catalytic reaction after 1 h, the AQY was calculated using the following equation:

$$AQY(\%) = \frac{N_e}{N_P} \times 100\% = \frac{\text{number of reacted electrons}}{\text{numbers of incident photos}} \times 100\%$$

$$= \frac{2 \times M \times N_A \times h \times c}{S \times P \times t \times \lambda} \times 100\%$$

Here, M is the number of CO molecules produced, S is the irradiation area, P is the irradiation intensity, t is the irradiation time, λ is the wavelength of monochromatic light, and N_A and h are the Avogadro and Planck constants, respectively.

2.14. Femtosecond transient absorption spectroscopy (FS-TAS)

The femtosecond time-resolved spectra of each sample were recorded using a Helios spectrometer (Ultrafast Systems). Before testing, 10 mg samples were evenly dispersed in 5 mL ethyl acetate under ul-

trasound. Then the dispersion was evenly dripped onto a glass sheet to form a uniform film. The glass sheet was then placed on the sample holder and the proper position was adjusted. A 400 nm pump pulse was generated as part of an 800 nm output using an optical parametric amplifier (OPerA Solo, Coherent). The pump light focused on the sample had a beam waist of approximately 360 μm and a power intensity of 200 μJ/cm^2. The changes in the signal were measured in the range of 0–1000 ps. The calculation of average emission lifetime was derived utilizing the following formula: $\tau_A = \frac{A_1\tau_1^2 + A_2\tau_2^2}{A_1\tau_1 + A_2\tau_2}$.

2.15. Positron annihilation lifetime spectral (PALS)

The PALS spectra of the samples were obtained using a fast–slow simultaneous generation system with a time resolution of 230 ps for the full-width-at-half-maximum. The samples were prepared by sandwiching the radioactive ^{22}Na source (3 μCi) between two identical samples covered with Al foil (diameter: 10.0 mm, thickness: 1.0 mm). Each sample was measured three times in parallel to obtain an average value at room temperature. One million counts were recorded for each spectrum. The experimental data obtained were analysed using Maestro software.

2.16. ^{13}C isotopic labeling experiment

^{13}C isotope tracing techniques were performed to identify the carbon sources of CH_4 and CO. Specifically, 15 mg of the catalyst was suspended in a mixture of water (25 mL) and acetonitrile (5 μL) in a closed quartz reactor. The temperature of the reactor was kept at 25 ℃ by circulating the condensate. The system was pumped to vacuum, and then high-purity CO_2 gas was passed into the reaction system. The radiation from a 300 W Xe lamp was passed through a 420 nm cut-off filter and used as a light source to illuminate the quartz reactor for 2 h. After the reaction, the gaseous products were qualitatively detected by gas chromatography–mass spectrometry.

3. Results and discussion

The $CABB/V_{Bi-O}BWO$ heterojunction photocatalyst was synthesised via a defect-confinement strategy of V_{Bi-O} BWO and CABB, as schematically illustrated in Fig. 1a. First, CABB quantum dots were prepared by reacting Cs-oleate with $BiBr_3$ and $AgNO_3$ (molar ratio of $BiBr_3$: $AgNO_3$: Cs-oleate was 2:2:1) in oleic acid (OA) and oleyl amine (OLA) as an organic solvent at 200 ℃. In addition, defective Bi_2WO_6 nanosheets were prepared by reacting the precursors BiOBr and WO_4^{2-} in a 1:2 molar ratio using a hydrothermal method. Powder X-ray diffraction (XRD) was used to explore the crystallinity and phase of the synthesised materials, where the patterns of $V_{Bi-O}BWO$ and CABB were indexed to the orthorhombic Bi_2WO_6 (JCPDS No. 73–2020) and cubic $Cs_2AgBiBr_6$ phases, respectively (Fig. S1) [28,29]. All of the characteristic XRD peaks of orthorhombic Bi_2WO_6 and cubic $Cs_2AgBiBr_6$ were also clearly identified in the $CABB/V_{Bi-O}BWO$ hybrid samples (Fig. S1). The crystal phase structure and morphology of the samples were further investigated using aberration-corrected scanning transmission electron microscopy (AC-STEM). The morphology of the CABB (Fig. 1b) shows regular quadrangular crystals with a size of 9 nm. The corresponding high-resolution STEM images show a clear lattice spacing of 0.291 nm corresponding to (004) crystal planes of $Cs_2AgBiBr_6$(Fig. 1c) [29]. Fig. 1d shows AC-STEM images of $V_{Bi-O}BWO$, which maintained a typical sheet-like structure without any morphological changes during the continuous hydrothermal process. The high-resolution STEM images of V_{Bi-O}-BWO nanosheets show that the interplanar spacings between the well-crystallized lattice fringes are 0.272 and 0.273 nm, which are attributed to the (020) and (200) [28,30]. Furthermore, fuzzy lattice fringes in the blue region are observed on the $V_{Bi-O}BWO$ surface, indicating the presence of abundant defects (Figs. 1e and S2a). The
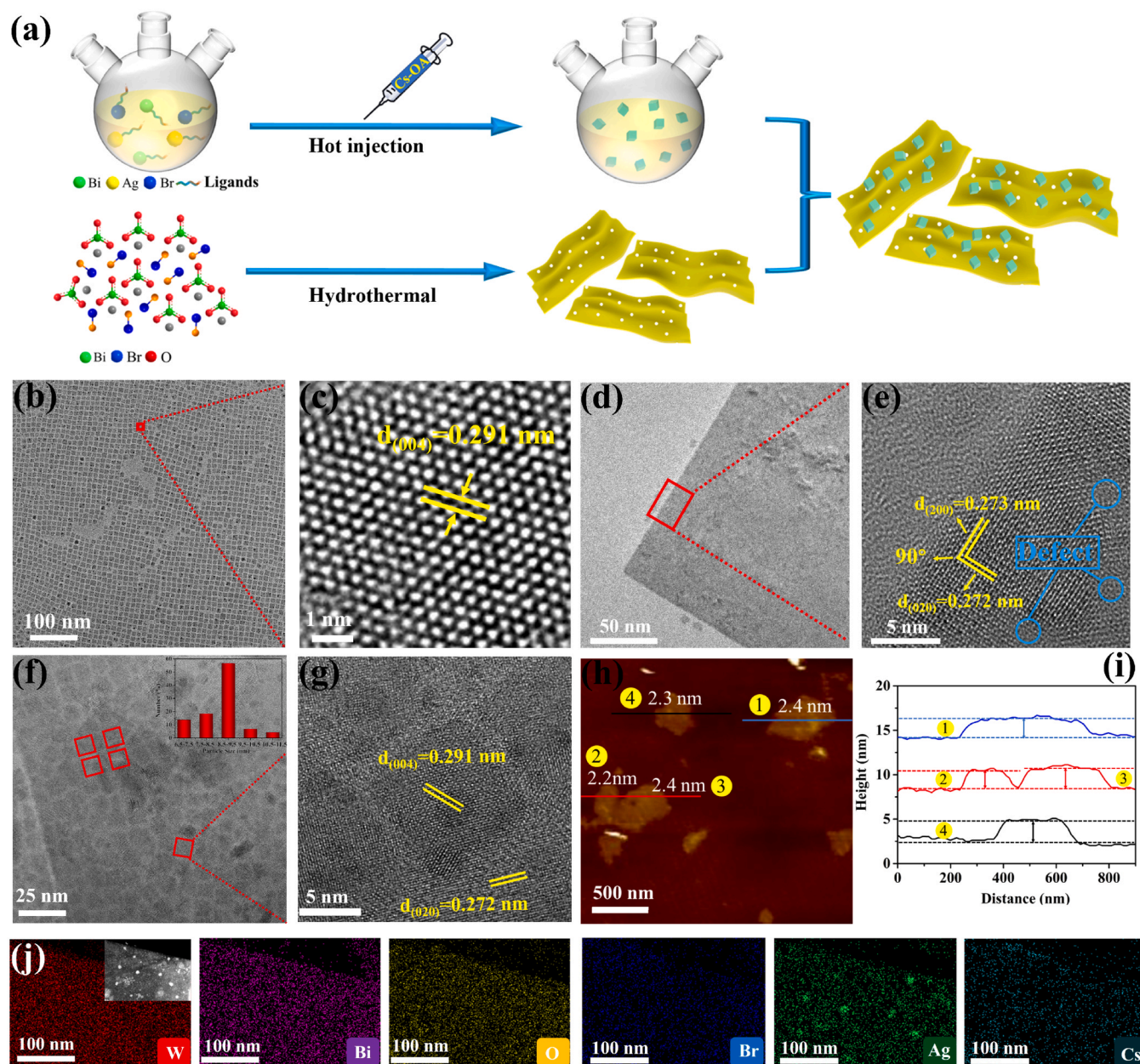
Fig. 1. Morphology of CABB, V_{Bi-O}BWO and 10CABB/V_{Bi-O}BWO heterojunction. (a) Synthesis schematic illustration for CABB/V_{Bi-O}BWO heterojunction. (b, c) STEM images of CABB. (d, e) STEM images of V_{Bi-O}BWO nanosheets. (f, g) STEM images of 10CABB/V_{Bi-O}BWO and corresponding size distribution (inset) of CABB quantum dots on the V_{Bi-O}BWO surface. (h) AFM image of a 10CABB/V_{Bi-O}BWO nanosheets and (i) the corresponding height profiles, the numbers 1–4 in (i) correspond to those in (h). (j) EDS elemental maps of 10CABB/V_{Bi-O}BWO.

corresponding intensity analysis of the atomic arrangement at the defect site showed a significant drop in the defect regions, which confirmed the existence of abundant defects (Fig. S2b). CABB quantum dots were deposited on V_{Bi-O}-BWO nanosheets using a defect-confinement strategy. Considering that the CABB surface is negatively charged (zeta potential −22.4 mV), while the V_{Bi-O}-BWO nanosheets are positively charged (zeta potential 24.2 mV) (Fig. S3a, b), the opposite surface charges promote the formation of a close interfacial contact between the CABB and V_{Bi-O}BWO nanosheets. As shown in Fig. 1f and Fig. S4, the CABB quantum dots are uniformly and closely anchored on the V_{Bi-O}BWO nanosheets. These sheet structures were functionalized with CABB, and their morphologies remained unchanged after surface modification. The high-resolution AC-STEM image shows a distinct interface between two intimately bonded materials with the interplanar d-spacing of 0.291 and 0.272 nm, respectively, which is in good

agreement with the (004) plane of CABB and the (020) plane of V_{Bi-O}BWO (Fig. 1g) [28–30]. These results indicate that heterojunctions were formed between CABB and V_{Bi-O}BWO. The corresponding energy-dispersive X-ray spectroscopy (EDS) spectra show that Cs, Ag, Bi, Br, W, and O are present in the 10CABB/V_{Bi-O}BWO hybrid nanosheets (Fig. 1j). Notably, Bi, W, and O were evenly distributed throughout the nanosheets, whereas Cs, Ag, and Br were only localised on the nanosheets, demonstrating that the CABB quantum dots were highly dispersed and tightly anchored to the surface of the V_{Bi-O}BWO nanosheets. Furthermore, atomic force microscopy (AFM) images of the as-prepared 10CABB/V_{Bi-O}BWO showed a lateral size of 500 nm and a vertical thickness of approximately 2 nm, demonstrating the characteristics of ultrathin nanosheets (Fig. 1h, i). The above characterisation results confirm the successful preparation of CABB/V_{Bi-O}BWO hybrid samples.

Raman, EPR, and XPS experiments were performed to explore the molecular structures, defect states, and interactions between the synthesised materials. As shown in the Raman spectra in Fig. S5a, two peaks at 178 and 135 cm^{-1} were assigned to the A_{1g} and E_g vibration modes of CABB, respectively, further indicating that the cubic CABB phase was formed [31,32]. The Raman spectrum of pure BWO (Fig. S5a) includes peaks at 795 and 825 cm^{-1}, corresponding to the asymmetric and symmetric A_g modes of the O–W–O group, respectively, while the peak at 715 cm^{-1} could be attributed to the antisymmetric bridging mode of the tungstate chain. Meanwhile, the peaks at 309 cm^{-1} are related to the translation modes of Bi^{3+} and WO_6^{6-} [33–35]. Compared to the Raman peaks of pure BWO, the corresponding peaks for $V_{Bi-O}BWO$ are significantly weaker and the peak at 303 cm^{-1} shifted to a lower wavenumber. This indicates the formation of defects, the substitution of defect-induced lattice distortion, and a lower degree of crystallinity. After the hybridisation with CABB, the Raman peaks of 10CABB/$V_{Bi-O}BWO$ are significantly weaker than those of $V_{Bi-O}BWO$ and BWO, revealing an interaction between CABB and $V_{Bi-O}BWO$ (Fig. S5a). EPR measurements provide valuable information on the formation of single electrons to guide the exploration of defects in single-electron capture. Symmetric EPR signals located at g=2.003 were observed for $V_{Bi-O}BWO$ and 10CABB/$V_{Bi-O}BWO$, which were assigned to vacancies (Fig. S5b) [36–38]. In contrast, no obvious signal was detected for BWO at g=2.003, indicating a perfect BWO structure. The enhanced signal intensity measured for 10CABB/$V_{Bi-O}BWO$ relative to that of $V_{Bi-O}BWO$ indicates a higher vacancy concentration in CABB/$V_{Bi-O}BWO$ (Fig. S5b). This is mainly due to the strong electron interactions between $V_{Bi-O}BWO$ and CABB.

The presence of defects and the interaction between CABB and $V_{Bi-O}BWO$ in the hybrid sample were further investigated by XPS. The XPS survey spectra (Fig. S6) show that the characteristic peaks in the 10CABB/$V_{Bi-O}BWO$ sample can be attributed to Cs, Ag, Bi, Br, O, and W, indicating the successful synthesis of 10CABB/$V_{Bi-O}BWO$ via a defect-confinement strategy. The binding energy peaks of Bi 4 f at 164.62 and 159.27 eV in pure BWO are attributed to Bi 4 $f_{5/2}$ and Bi 4 $f_{7/2}$, respectively (Fig. S7a) [39,40]. Interestingly, the binding energies of Bi 4 $f_{5/2}$ and 4 $f_{7/2}$ in V_{Bi-O} BWO shift towards lower binding energy compared with that of pure BWO, illustrating the changed chemical state of Bi^{3+} in $V_{Bi-O}BWO$ owing to the defect structure. After the hybridisation with CABB, the high-resolution spectra of Bi 4 $f_{7/2}$ (158.97 eV) and Bi 4 $f_{5/2}$ (164.29 eV) measured for CABB/$V_{Bi-O}BWO$ were significantly shifted to lower binding energies than those of Bi 4 $f_{7/2}$ (159.17 eV) and Bi 4 $f_{5/2}$ (164.51 eV) in $V_{Bi-O}BWO$ (Fig. S7a). A similar negative shift appeared in the W 4 f spectrum of the sample, and the W 4 f XPS spectrum of BWO shows two peaks at 37.81 and 35.78 eV, which are attributed to W 4 $f_{5/2}$ and W 4 $f_{7/2}$, respectively (Fig. S7b) [41,
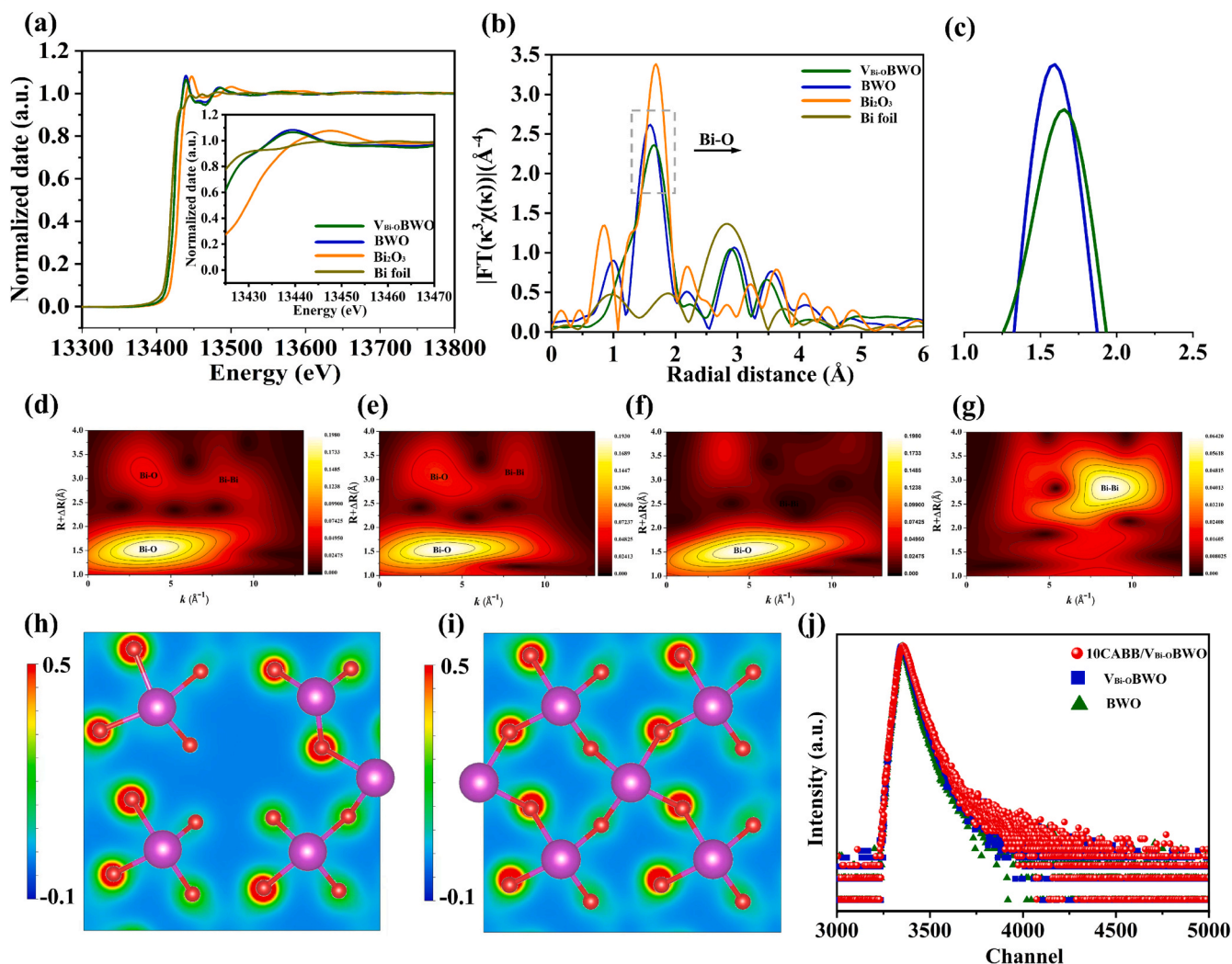

Fig. 2. (a) XANES Bi L_3 edge spectra, (b, c) Bi k^3-weighted R-space Fourier-transform EXAFS spectra, and (d-g) Bi K-edge wavelet-transformed EXAFS spectra for $V_{Bi-O}BWO$, BWO, Bi_2O_3, and Bi foil. (h, i) Electron density images of $V_{Bi-O}BWO$ and BWO obtained by DFT calculations. (j) Positron annihilation spectra of 10CABB/$V_{Bi-O}BWO$, $V_{Bi-O}BWO$, BWO.

42]. A significant shift towards lower binding energies is observed for the $W4f_{5/2}$ and $W4f_{7/2}$ peaks in $V_{Bi-O}BWO$ relative to those in BWO, which indicates a change in the electron cloud density of W due to the presence of defects. For $10CABB/V_{Bi-O}BWO$, these peaks are located at lower binding energies than those of $V_{Bi-O}BWO$ (35.58 and 37.61 eV) (Fig. S7b). In contrast, for the $10CABB/V_{Bi-O}BWO$ heterojunction, Ag and Cs become electron-deficient; to balance the electron redistribution in $10CABB/V_{Bi-O}BWO$, Bi and W in $10CABB/V_{Bi-O}BWO$ should be electron-rich. As shown in Fig. S7d, the binding energies of Cs $3d_{5/2}$ (724.28 eV) and Cs $3d_{3/2}$ (738.22 eV) in $10CABB/V_{Bi-O}BWO$ are higher than those of pure CABB by 0.3 eV [40,43]. Similarly, the binding energies of Ag $3d_{5/2}$ and Ag $3d_{3/2}$ occur at 368.02 and 374.04 eV, respectively, for $10CABB/V_{Bi-O}BWO$ (Fig S7c), and these peaks are located at higher binding energies relative to pure CABB (367.73 and 373.73 eV, respectively) [44]. These results demonstrate the formation and electron migration of heterojunctions between CABB and $V_{Bi-O}BWO$.

X-ray absorption fine structure (XAFS) spectra were obtained to explore defect configurations, surface chemical valence states, and atomic arrangements. As shown in Fig. 2a, the Bi K-edge X-ray absorption near-edge structure (XANES) spectra for $V_{Bi-O}BWO$ and BWO display characteristics similar to those of the Bi_2O_3 standard sample, indicating a similar electronic structure. Significantly, the energy of Bi in BWO samples indicated in the XANES spectrum shifts to a lower energy of 13439 eV relative to that of Bi_2O_3 (13448 eV), indicating a reduced oxidation state ($Bi^{\delta+}$, $0 < \delta < 3$) relative to Bi^{3+} in Bi_2O_3. Compared with BWO, the weakened XANES intensity of $V_{Bi-O}BWO$ indicates a further reduction in the oxidation states. This can be explained by the formation of defects in $V_{Bi-O}BWO$, as confirmed by XPS. The Fourier-transform (FT) K^3-weighted EXAFS spectra of the sample are shown in Fig. 2b, c. The Bi K-edge R space spectrum of $V_{Bi-O}BWO$ shows oscillating curves at 1.5 Å, which are assigned to Bi–O first shells, respectively [45,46]. Notably, the peak intensity of Bi–O for $V_{Bi-O}BWO$ is significantly lower than that of BWO. This suggests that the reduction of Bi and O coordination numbers in $V_{Bi-O}BWO$ is due to the formation of Bi-O defects. Concurrently, the oscillation curve attributed to the Bi–O bonds of $V_{Bi-O}BWO$ shifted to higher (0.08 Å) R direction values compared to those of BWO, indicating a distorted microstructure caused by the Bi–O defects. EXAFS wavelet transforms (EXAFS-WTs) provide 3D visualisations of EXAFS spectra by presenting signals in the K and R spaces (Fig. 2d-g). The WT-EXAFS contour map of $V_{Bi-O}BWO$ highlights an obvious maximum (R=1.65 Å, K=4.0 Å^{-1}), which belongs to the Bi–O scattering paths. The WT-EXAFS contour map of $V_{Bi-O}BWO$ highlights obvious signals located at R= 1.65 Å, K= 4.0 Å^{-1} and R= 2.87 Å, K= 4.0 Å^{-1}, respectively, which belongs to the Bi–O scattering paths. However, the signal at R=3.5 Å and K=8.2 Å^{-1} belongs to the Bi-Bi scattering path. Therefore, the Bi K-edge R space spectrum of $V_{Bi-O}BWO$ shows oscillating curves at 3.5 Å, which are assigned to Bi-Bi shell. Obviously, the peak intensities of Bi–Bi for $V_{Bi-O}BWO$ are significantly lower than those of BWO. This suggests that the reduction in the Bi coordination numbers is due to the formation of Bi–O defects in $V_{Bi-O}BWO$. Fig. S8 and Fig. S9 are sample fitting curves in K and R space, respectively, the fitting results are in agreement with the original data via the least squares method for all samples in the K and R spaces, and the quantitative structural parameters around Bi atoms restricted in BWO and $V_{Bi-O}BWO$ are shown in Table S1. The coordination numbers of Bi-O1, Bi-O2 and Bi-Bi1 in $V_{Bi-O}BWO$ are significantly reduced compared with that of pure BWO. These indicates that the loss of adjacent Bi-O atomic pairs in the Bi-O shell and Bi-Bi layer did not cause significant changes in the monolayer structure, but leads to the formation of Bi-O vacancy pairs. To further study the stable configuration of the $V_{Bi-O}BWO$ nanosheets, we calculated the electron density distributions of BWO and $V_{Bi-O}BWO$ samples using density functional theory (DFT). As shown in Fig. 2h, i, the loss of bridging Bi–O atoms was conducive to stabilising $V_{Bi-O}BWO$. The existence of Bi–O defects may lead to the distortion of the atomic structure and redistribution of charge in $V_{Bi-O}BWO$. There is obvious charge consumption (from red to blue) around the Bi^{3+} ion originally bonded to it, which is due to the

uncoordinated hanging bond in the direction of the missing Bi and O atom. The absence of Bi and O atoms can effectively enhance the adsorption performance of nearby Bi atoms for CO_2 with the characteristics of a Lewis acid. The above conclusions prove that bridging Bi–O defects exist in $V_{Bi-O}BWO$.

The defect structures and concentrations in BWO, $V_{Bi-O}BWO$, and $10CABB/V_{Bi-O}BWO$ were compared using positron annihilation lifetime spectrometry (PALS), which is a well-established technique for revealing local microstructural changes in samples. As shown in Fig. 2j and Table S2, the measured PALS lifetime profiles show a three-part attenuation for all tested samples. The shortest decay step of τ_1 is related to the oxygen vacancies in the sample, whereas the second step of τ_2 is assigned to positrons capturing the Bi–O vacancy pairs. The longest step of τ_3 is attributed to large holes [47,48]. Significantly, τ_1 and τ_2 for $V_{Bi-O}BWO$ (226.8 and 325.3 ps, respectively) and $CABB/V_{Bi-O}BWO$ (238.2 and 338.5 ps, respectively) are higher than those for pure BWO (195.9 and 302.1 ps, respectively). More importantly, the relative intensity of all the PALS lifetime components was proportional to the defect concentration. The values of I_2 are 57.7% for $10CABB/V_{Bi-O}BW$ and 50.6% for $V_{Bi-O}BWO$, respectively, which are significantly higher than those of pure BWO (Table S2). Based on the above analysis, an effective structural model was developed to study the relationship between the double defect-confinement quantum dots and the photocatalytic performance.

The photocatalytic performances of the samples for CO_2 reduction were measured in a closed gas-cycle installation using a quartz and glass hybrid reactor (Labsolar-6a) (Fig. S10). All prepared samples exhibited significant visible light absorption based on their diffuse reflectance spectra (DRS) (Fig. S11). Therefore, a 300 W Xe arc lamp was equipped with a 420 nm cutoff filter as the visible light source. For all experimental tests, CO was analysed as the main product, accompanied by certain concentrations of CH_4 and O_2 (Fig. 3b-c). Among the samples, pure CABB and BWO showed relatively low CO (4.2 and 2.2 μmol/g, respectively) and CH_4 (0.4 and 0.8 μmol/g, respectively) production rates due to fast charge recombination in the single materials. When Bi–O double defects were introduced, the CO, CH_4, and O_2 yields of $V_{Bi-O}BWO$ are 4, 2.5, and 4 times higher than those of the pure BWO, respectively ((Fig. 3a-b)). This is mainly due to the presence of defects that can accelerate the charge transfer and activation of reactive molecules. With CABB loading (e.g., 5%), the CO, CH_4 and O_2 production rates increase to 18.4, 4.2, and 8.6 μmol/g, respectively, indicating that the formation of hybrid materials can accelerate the formation of products. The photocatalytic activity of $CABB/V_{Bi-O}BWO$ increased significantly with increasing CABB content. The $10CABB/V_{Bi-O}BWO$ with an optimal CABB loading of 10% achieved the highest CO (48.5 mol/g/h), CH_4 (7.2 μmol/g/h) and O_2 (23.6 μmol/g/h) yields after 4 h of visible light irradiation, which are 22, 9 and 20 times higher than those of pure BWO, respectively (Table S3).

However, when the content of CABB in the hybrid reached 12.5 wt% (i.e. $12.5CABB/V_{Bi-O}BWO$), the yields of all products decreased significantly, indicating that an excessive concentration of CABB negatively affected the performance of the hybrid material. Furthermore, the total yield of CO reached 204.2 μmol/g, accompanied by the detection of methane (27.1 μmol/g) and oxygen (99.2 μmol/g) in the photocatalytic activity test of $10CABB/V_{Bi-O}BWO$ samples over twenty consecutive hours (Fig. 3d). These values are significantly higher than previously reported results. In the photocatalytic CO_2 reduction system, photoinduced electron-driven CO_2 reduction is associated with hole-dominated water oxidation ($2 H_2O + 4 h^+ \rightarrow O_2 + 4 H^+$). Theoretically, water oxidation continues to provide protons to assist the photogenic charge in reducing CO_2 to CO ($CO_2 + 2e^- + 2 H^+ \rightarrow CO + H_2O$) via the inherent photocatalytic CO_2 reduction pathway. The experimentally measured CO/O_2 yield over the samples closely matches the theoretical yield (2:1) assuming $2CO_2 \rightarrow 2CO + O_2$, which implies that water is the sacrificial electron donor of the hole to achieve the overall conversion of CO_2 and water (Fig. 3a, c). Considering the reaction kinetics, this is attributed to
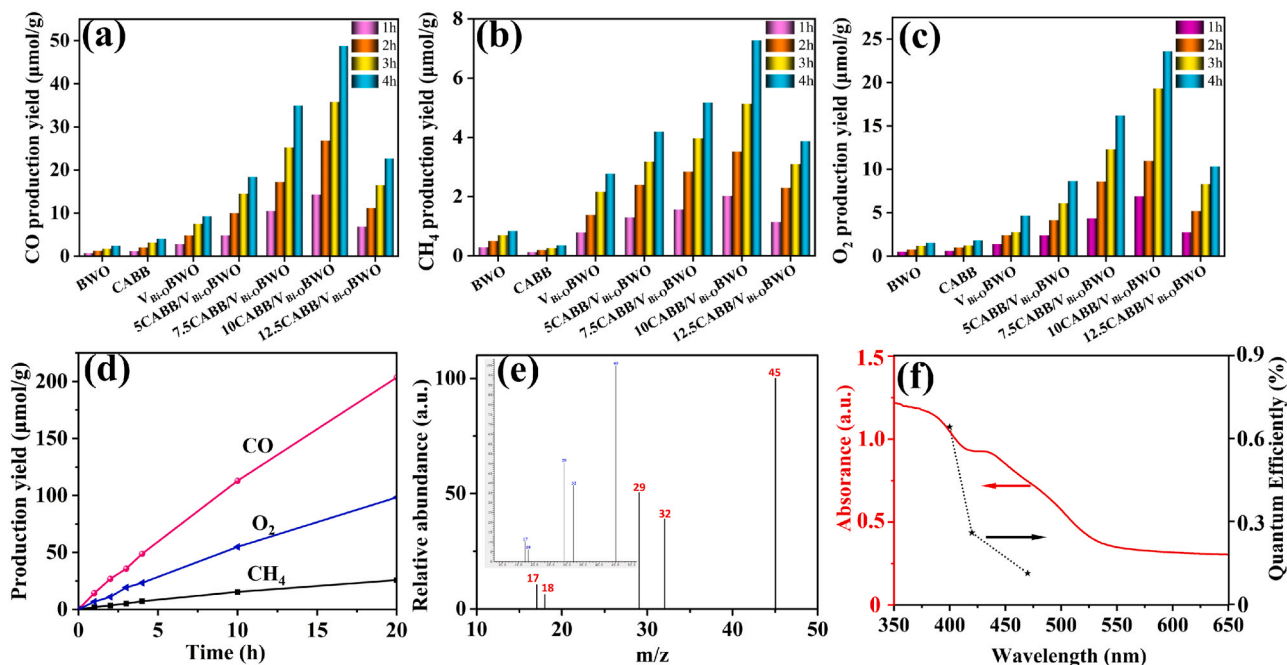
Fig. 3. Photocatalytic activities of CO_2 reduction over BWO, CABB, V_{Bi-O}BWO, 5CABB/V_{Bi-O}BWO, 7.5CABB/V_{Bi-O}BWO, 10CABB/V_{Bi-O}BWO, and 12.5CABB/V_{Bi-O}BWO during 4 h experiments performed under visible light irradiation: time course of (a) CO, (b) CH_4, and (c) O_2 production yields. (d) Continuous CO, CH_4, and O_2 generation over 10CABB/V_{Bi-O}BWO under visible light irradiation for 20 h. (e) Mass spectra of ^{13}CO and original total mass spectrum (inset) recorded during the photocatalytic reduction of $^{13}CO_2$ over 10CABB/V_{Bi-O}BWO. (f) Apparent quantum yield of CO production over 10CABB/V_{Bi-O}BWO under different wavelengths of monochromatic light during the photocatalytic CO_2 reduction process.

the reaction preferentially following a two-electron transfer mechanism.

A control experiment was performed to eliminate interference in the reaction, as shown in Fig. S12a. No products were detected in the absence of light, the catalyst, or CO_2, indicating that CO and CH_4 were produced by CO_2 photoreduction in the presence of the catalyst. To further trace the carbon source of the CO_2 photoreduction products, isotope-labelled $^{13}CO_2$ photocatalytic reduction measurements were performed. As shown in Fig. 3e, the mass spectrum signals at $m/z=29$ and 17 are attributed to ^{13}CO and $^{17}CH_4$, respectively, which strongly confirms that CO and CH_4 were derived from the photoreduced substrate CO_2. Mass signals attributed to H_2O ($m/z=18$) and O_2 ($m/z=32$) were also observed, indicating that O_2 was derived from the oxidation of water over CABB/V_{Bi-O}BWO. The apparent quantum yield (AQY) varies with wavelength. As shown in Fig. 3f, the AQY values for CO generation over 10CABB/V_{Bi-O}BWO were 0.64% at 400 nm, 0.26% at 420 nm, and 0.11% at 470 nm (Fig. 3f). The trend in the AQY over 10CABB/V_{Bi-O}BWO is closely related to its photoabsorption spectrum, which proves that the photoabsorption capacity is essential for improving the photocatalytic CO_2 reduction efficiency. The photocatalytic cycling performances and stabilities of the samples for CO_2 reduction were evaluated under identical conditions. After five cycles, the yields of CH_4, CO, and O_2 hardly decreased (Fig. S12b). In addition, the catalysts were characterised by Raman, XPS, and STEM before and after the reaction (Fig. S12c, d and Fig. S13a, b). The Raman results show that the crystal phase of the catalyst was similar before and after the reaction. The XPS results revealed that the valence states of W remained unchanged throughout the reaction. Furthermore, 10CABB/V_{Bi-O}BWO maintained a highly dispersed nanosheet morphology. These results show that the surface defects on V_{Bi-O}BWO can serve as an interface to stabilise the CABB on the surface, resulting in superior photocatalytic stability.

To elucidate the mechanism underlying the high yield of the CABB/ V_{Bi-O}BWO samples for photocatalytic CO_2 reduction, we conducted a convincing measurement. Typical photocatalytic CO_2 reduction involves the following three processes: (1) adsorption and activation of reactive molecules on the surface of the catalyst; (2) photoabsorption to

generate charge carriers that efficiently migrate between hybrid materials; and (3) reaction of the activated species with photoexcited electrons to form the final product. Considering that CO_2 and H_2O molecules act as substrates, the micro-coordination structure between H_2O molecules and 10CABB/V_{Bi-O}BWO was first investigated using in situ Raman spectroscopy (Fig. S14). As shown in Fig. 4a, the Raman spectra indicate that 10CABB/V_{Bi-O}BWO can be indexed as pure BWO. When interacting with water, a broad Raman peak at 2900–3700 cm^{-1} assigned to the O–H vibration of water molecules was detected under dark conditions. Notably, the peak was deconvoluted into two distinct components located at 3202 and 3437 cm^{-1} under light irradiation, which are attributed to 4-coordinated hydrogen-bonded water and hydrogen-bonded water adsorbed on the surface of 10CABB/V_{Bi-O}BWO, respectively [49]. Under light irradiation, the intensity of the 4-coordinated hydrogen-bonded vibration peak is significantly enhanced and the 2-coordinated hydrogen-bonded vibration peak shifts to a higher wavenumber (3350 cm^{-1}) compared with measured in the dark (Fig. 4a, b). This indicates that light can effectively drive the adsorption, activation, and coordination of water molecules on the catalyst surface, which is conducive to subsequent protonation. As expected, the contact angles of BWO and V_{Bi-O}BWO were determined to be 73° and 128° (Fig. S15a, b), respectively, indicating poor wettability due to weak interactions. When CABB was introduced, the contact angle of CABB/V_{Bi-O}BWO decreased to 25° (Fig. S15c), indicating a more hydrophilic surface that facilitates the water adsorption and accelerates the protonation reaction.

The interactions between CO_2 molecules and the sample were explored using CO_2-TPD experiments. As shown in Fig. 4c, the CO_2-TPD of 10CABB/V_{Bi-O}BWO comprises two strong CO_2 desorption peaks at 85 and 175 °C. However, no significant CO_2 desorption peaks were detected in the range of 0–200 °C for either V_{Bi-O}BWO or BWO samples. Furthermore, as the temperature increases, 10CABB/V_{Bi-O}BWO exhibits enhanced CO_2 desorption peaks at 348, 424, 776 and 836 °C, attributed to the chemical adsorption of CO_2 on the sample. Weak CO_2 adsorption peaks are observed for V_{Bi-O}BWO, while BWO exhibited a negligible response [50,51]. These results prove that the multifunctional active
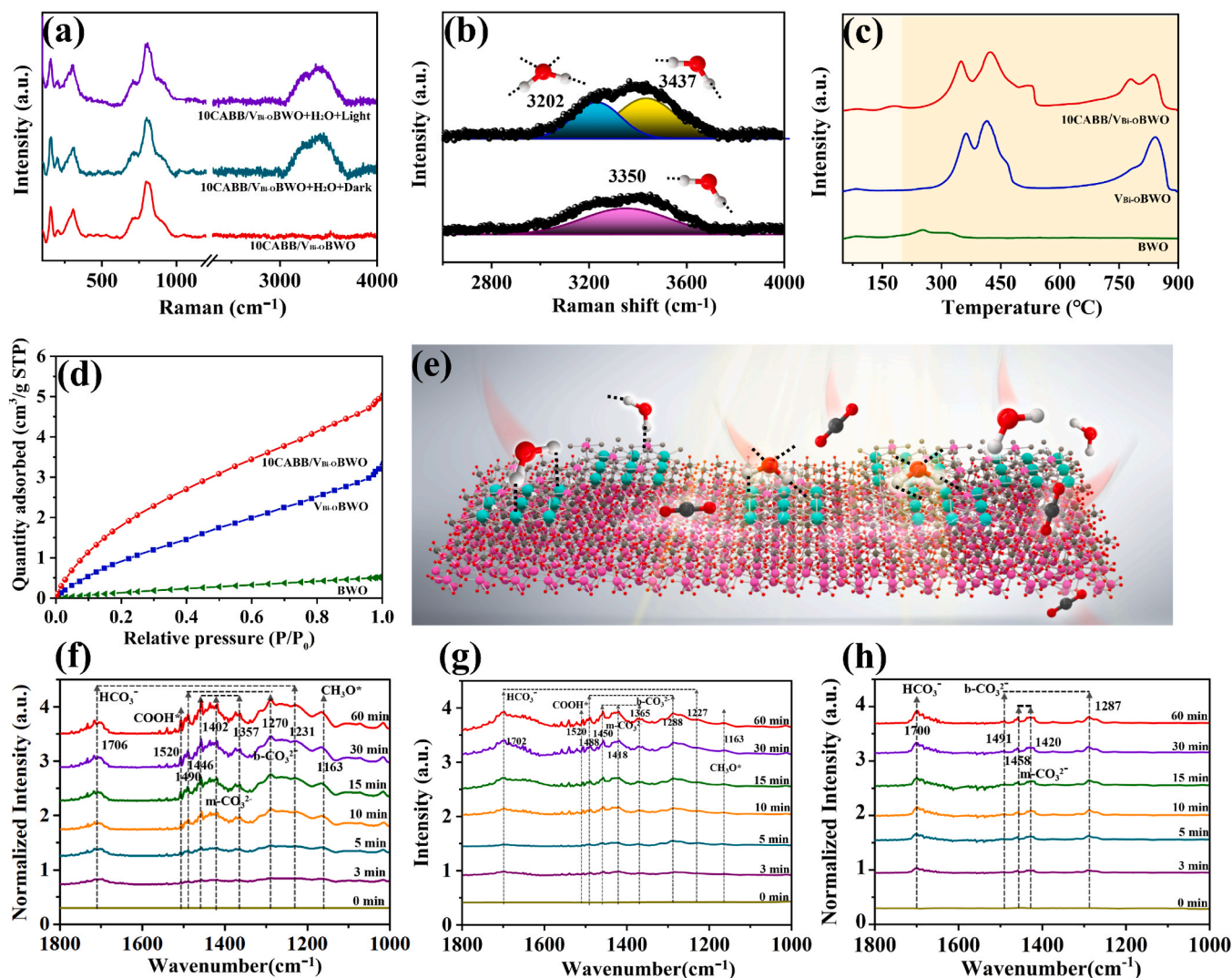
Fig. 4. (a) In situ Raman spectra of 10CABB/V_{Bi-O}BWO with adsorbed H_2O under light irradiation. (b) magnified views of the range of 2600–4000 cm^{-1} in (a). (c) CO_2-TPD of 10CABB/V_{Bi-O} BWO, V_{Bi-O}BWO and BWO. (d) CO_2 adsorption isotherms of 10CABB/V_{Bi-O}BWO, V_{Bi-O}BWO and BWO at 297 K. (e) Diagram of the adsorption mechanism of H_2O and CO_2 molecules on the catalyst surface. (f-h) In situ DRIFTS spectra a mixture of CO_2 and H_2O vapour on 10CABB/V_{Bi-O}BWO, V_{Bi-O}BWO and BWO.

sites on the surface of 10CABB/V_{Bi-O}BWO are conducive to the adsorption of CO_2. Moreover, the CO_2 adsorption capacity of samples was further investigated via the CO_2 adsorption isotherms at 297 K. As shown in Fig. 4d, 10CABB/V_{Bi-O}BWO showed the optimal CO_2 adsorption capacity compared to that of V_{Bi-O}BWO and BWO. Subsequently, in situ diffuse reflectance infrared fourier transform spectroscopy (In Situ DRIFTS) was performed to gain in-depth insight into the reaction intermediate species formed on the catalyst during photocatalytic CO_2 reduction. As shown in Fig. 4f, the FTIR spectrum of the 10CABB/V_{Bi-O}BWO samples comprises peaks at 1270 and 1490 cm^{-1} that are assigned to bidentate carbonate (B-CO_3^{2-}) species, while the peaks located at 1446, 1402 and 1357 cm^{-1} are assigned to monodentate carbonate (M-CO_3^{2-}) species [16,52–54]. Evidence of the formation of surface bicarbonate species (HCO_3^- at 1706 cm^{-1}) during photocatalytic CO_2 reduction was observed. Concurrently, the key intermediate species COOH* at 1520 cm^{-1} was also significantly detected. The infrared peaks attributed to monocarbonate, bicarbonate, bicarbonate species and COOH* were significantly enhanced with prolonged light irradiation, indicating that continuous light-assisted CO_2 reduction occurred on the surface of the CABB/V_{Bi-O}BWO samples. In contrast, in situ DRIFTS of the V_{Bi-O}BWO and BWO samples was performed under the same

conditions (Fig. 4g, h). During the CO_2 reduction reaction, the peaks belonging to the carbonate and bicarbonate species were significantly weaker for V_{Bi-O}BWO and BWO compared to those of 10CABB/V_{Bi-O}BWO, indicating the poor CO_2 adsorption–reactivation–conversion capacity for V_{Bi-O}BWO and BWO. Therefore, in situ DRIFTS provides strong evidence that the enhanced photocatalytic CO_2 reduction activity of 10CABB/V_{Bi-O}BWO is due to the accelerated formation of important intermediate species (B-CO_3^{2-}, M-CO_3^{2-}, HCO_3^- and COOH*) under continuous light irradiation.

Combined with the theoretical understanding of the transition state pathway of the catalyst during photocatalytic CO_2 reduction at the atomic level, the high yield of CO generated by CABB/V_{Bi-O}BWO was studied using DFT calculations (Fig. S16). Based on the aforementioned material characterisation results, we optimised and obtained three crystal structures representing the possible geometric coordinations of BWO, V_{Bi-O}BWO, and CABB/V_{Bi-O}BWO, for photocatalytic CO_2 reduction calculations (Fig. S17). The DFT calculation results in Fig. 5a-c show that the three samples have similar intermediate free energy distributions, but the change in the intermediate free energy has the lowest energy pathway for CABB/V_{Bi-O}BWO during photocatalytic CO_2 reduction (Fig. 5a). The rate-limiting step for CO generation is considered to
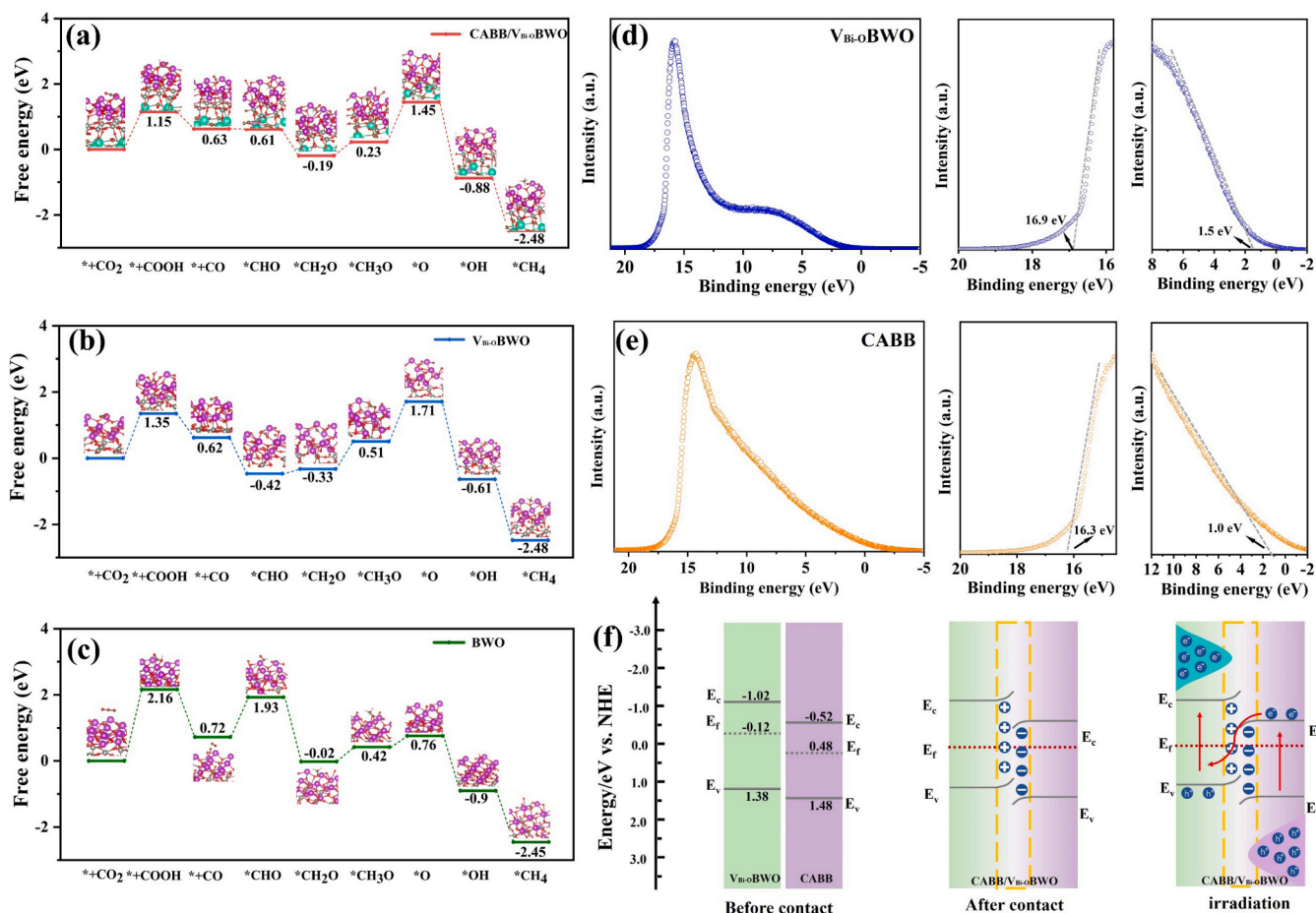
Fig. 5. (a-b) Free energy diagrams of CO_2 photoreduction to CO and CH_4 over CABB/V_{Bi-O}BWO, V_{Bi-O}BWO, and BWO. (d-e) UPS spectra of V_{Bi-O}BWO and CABB. (f) Schematic illustration of the formation and working mechanism of Z-scheme in CABB/V_{Bi-O}BWO heterojunction.

be CO_2 protonation to *COOH in all samples. CABB/V_{Bi-O}BWO possessed the lowest COOH* formation energy (1.15 eV) compared to V_{Bi-O}BWO (1.35 eV) and BWO (2.16 eV). Subsequently, the *COOH intermediate species split into *CO and H_2O in the presence of protons. This may be because the introduction of CABB led to an increase in the electron cloud density in V_{Bi-O}BWO and the formation of multifunctional reactive active centres. Therefore, compared to pure V_{Bi-O}BWO and BWO, CABB/ V_{Bi-O}BWO can more effectively promote the formation of COOH* intermediates, thereby achieving a high catalytic activity for CO. Furthermore, CHO* intermediates are more likely to form on the surface of the CABB/V_{Bi-O}BWO and V_{Bi-O}BWO samples than on pure BWO, which may contribute to greatly reducing the CHO* generation energy in CABB/V_{Bi-O}BWO and BWO because CO* hydrogenation to CHO* is a spontaneous process (Fig. 5a-c). In contrast, the subsequent protonation of CHO* until the final formation of CH_4 requires a rigorous, nonspontaneous pathway (Fig. 5a-c). This indicates that CH_4 formation is not the preferred pathway for the prepared samples, which is consistent with the small amount of CH_4 detected during the photocatalysis experiments (Fig. 3b). Therefore, there is a theoretical basis explaining why CABB/V_{Bi-O}BWO is more conducive to the formation of CO during photocatalytic CO_2 reduction than BWO and V_{Bi-O}BWO, which is consistent with the activity tests and previous characterisation results.

Photoinduced interfacial charge transfer requires the matching of suitable energy levels at the heterojunction interface to achieve efficient photocatalytic CO_2 reduction. In our case, this depends on the Fermi levels of the V_{Bi-O}BWO and CABB components. Therefore, we used Tauc plots, XPS valence band spectra, and ultraviolet photoelectron spectroscopy to determine the band structures of V_{Bi-O}BWO and CABB. Based

on the linear intersection rule, the maximum valence band energy (E_{VB}) of V_{Bi-O}BWO and CABB were determined to be 1.53 eV and 1.07 eV (vs. normal hydrogen electrode (NHE)), respectively (Fig. S18). The valence band values of V_{Bi-O}BWO and CABB were calculated as 1.38 and 1.48 eV vs. NHE, respectively. Correspondingly, the conduction band energy (E_{CB}) of V_{Bi-O}BWO and CABB were calculated as −1.02 and −0.52 eV vs. NHE, respectively using the relationship $E_{CB}=E_{VB}-E_g$, where E_g is the bandgap energy [55,56]. In addition, the Fermi level (E_f) values of V_{Bi-O}BWO and CABB determined from UPS and XPS valence band spectroscopy were calculated as −0.12 and 0.48 eV vs. NHE, respectively (Fig. 5d, e and Fig. S18). Because the charge-transfer process on the semiconductor heterojunction interface depends on the E_f values, the electrons in the CABB flow through the out-of-phase junction to the V_{Bi-O}BWO until their E_f values reach equilibrium. Therefore, the interfacial region near V_{Bi-O}BWO accumulates a positive charge owing to the outflow of electrons, and the interfacial region of CABB remains a negative charge. An internal electrostatic field from CABB to V_{Bi-O}BWO is formed at the heterojunction interface, which contributes to the spatial separation of photoelectron–hole pairs and promotes carrier transfer through the Z-scheme path owing to band bending (Fig. 5f).

Our previous work demonstrated that in situ XPS under light irradiation of the catalysts can be used to explore the migration pathway of photogenerated charges and holes between hybrid materials by analysing the changes in the electron cloud density of elements before and after irradiation (Fig. S19). As shown in Fig. 6a, the binding energies of Cs $3d_{3/2}$ (738.42 eV) and Cs $3d_{5/2}$ (724.52 eV) for CABB/V_{Bi-O}BWO under light irradiation were shifted by 0.22 eV to higher binding energies compared with those obtained under dark condition. Conversely,
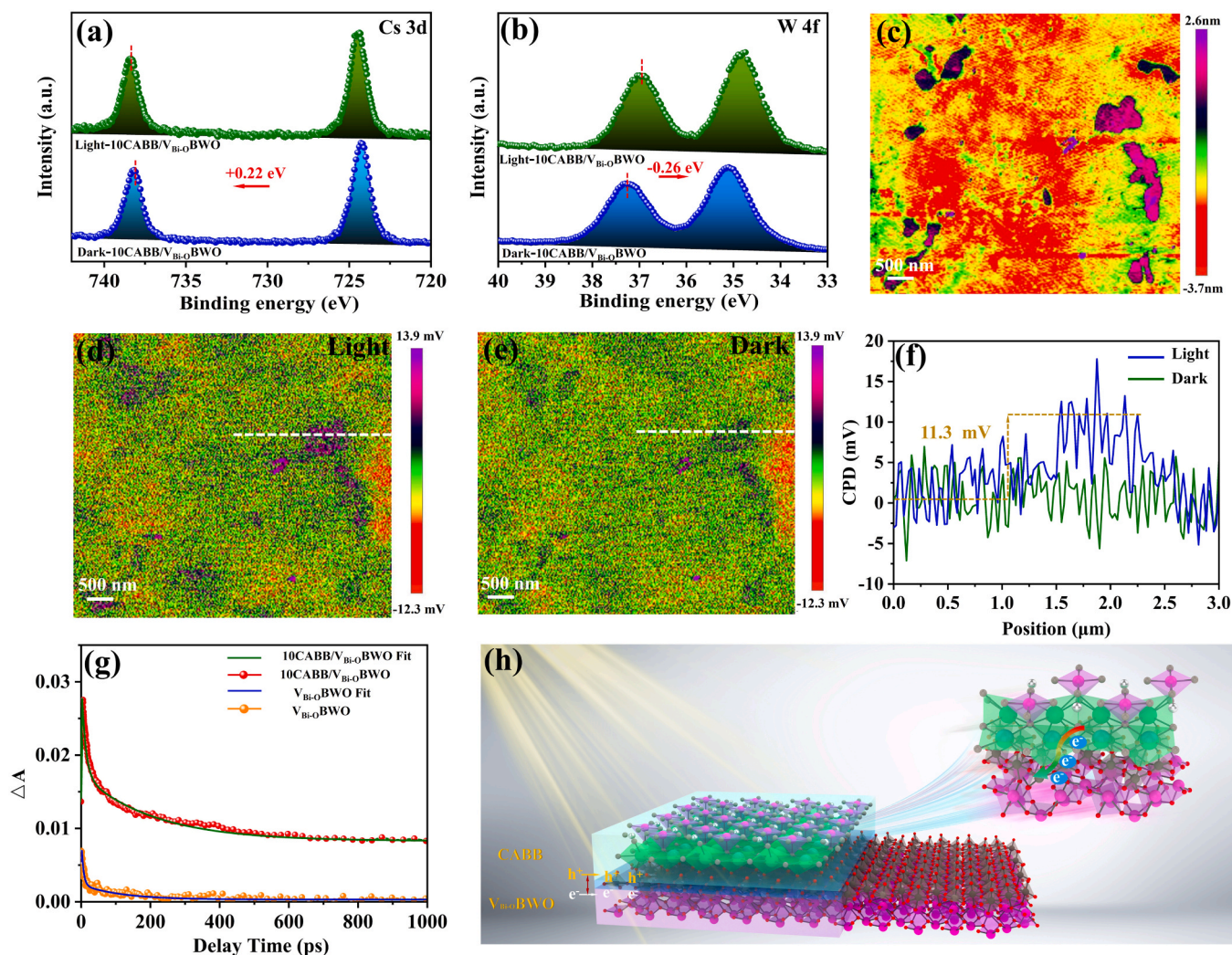
Fig. 6. (a-b) In situ XPS spectra of Cs 3d and W 4 f in the 10CABB/V_{Bi-O}BWO sample under dark conditions and irradiation at 402 nm. (c) AFM height image of 10CABB/V_{Bi-O}BWO. (d-f) Surface potential images in the light, under dark, and the corresponding line profiles of surface potential. (g) TA kinetic plots of 10CABB/V_{Bi-O}BWO and V_{Bi-O}BWO monitored at 520 nm. (h) Schematic diagram of charge transfer mechanism in CABB/V_{Bi-O}BWO Z-scheme heterojunction.

the binding energies of W 4 $f_{5/2}$ and W 4 $f_{7/2}$ were observed at 37.23 and 35.14 eV, respectively, for CABB/V_{Bi-O}BWO under dark conditions, which both shifted 0.26 eV toward lower binding energies under light irradiation (Fig. 6b). This indicates that the local electron cloud density of W increases, whereas that of Cs decreases owing to photogenerated charge migration from CABB to V_{Bi-O}BWO. The migration pathways of the spatially resolved photogenerated carriers on CABB/V_{Bi-O}BWO were comprehensively explored using in situ irradiation-assisted KPFM. The AFM image shows that the CABB/V_{Bi-O}BWO sample has an ultrathin nanosheet morphology, which is consistent with that shown in the STEM images (Fig. 1f, h). Therefore, this region was selected for this study. Fig. 6d and e show the KPFM images and corresponding surface photovoltage (SPV) difference tangent plots of the V_{Bi-O}BWO samples under light and dark conditions, respectively. No significant SPV signal was detected under dark conditions because of the lack of light stimulation, whereas a significant SPV signal was detected under light irradiation (Fig. 6d, e). The potential difference between the 10CABB/V_{Bi-O}BWO samples under light and dark conditions was 11.3 mV (Fig. 6f). The photo-driven charge mapping and SPV signal difference diagrams strongly demonstrate the effective charge transfer at the 10CABB/V_{Bi-O}BWO interface. The relaxation dynamic behaviour of time-resolved photogenerated carriers on samples was comprehensively explored by femtosecond time-resolved transient absorption spectroscopy. Fig. 6g

shows the decay kinetic curves of 10CABB/V_{Bi-O}BWO and V_{Bi-O}BWO, among which 10CABB/V_{Bi-O}BWO had the fastest attenuation rate. Specifically, 10CABB/V_{Bi-O}BWO exhibited a minimum average decay time (250 ps) that was shorter than those of CABB (7291 ps). Typically, the short-lifetime (t_1) and long-lifetime (t_2) components are caused by electrons trapped in shallow and deep traps, respectively, before recombination (Fig. 6c and Table S4). This demonstrates that the ultrathin CABB/V_{Bi-O}BWO 0D/2D heterogeneous interface significantly accelerates charge transfer and separation. According to the above analysis, the enhanced photocatalytic activity of CABB/V_{Bi-O}BWO is due to the efficient charge transfer based on temporal and spatial resolution scales.

The effective separation and migration abilities of the photogenerated electrons and holes in the sample were further investigated via photoelectrochemical characterization to demonstrate the efficient catalytic performance of 10CABB/V_{Bi-O}BWO based on semiconductor band theory. The transient photocurrent response curve of the sample under intermittent irradiation is presented in Fig. S20a. Normally, the photoresponse intensity typically exhibits a positive correlation with the efficiency of electron-hole separation, thereby indicating an enhanced performance. It can be seen from the figure that the photocurrent intensity of V_{Bi-O}BWO is twice higher than that of BWO, thereby substantiating the enhancement in photogenerated charge migration

resulting from the introduction of defect levels. The highest photocurrent intensity for 10CABB/BWO relative to that of V_{Bi-O}BWO and BWO indicates a more efficient migration of charges from CABB to BWO. Linear sweep voltammetry (LSV) curves were obtained to investigate the overpotential of hydrogen formed by the hydrolysis of the samples. As shown in Fig. S20b, the lowest hydrogen production overpotential was obtained for the 10CABB/V_{Bi-O}BWO sample relative to those of V_{Bi-O}BWO and BWO, which strongly proves that 10CABB/V_{Bi-O}BWO is more effective for providing a hydrogen source for the CO_2 reduction process. The cyclic voltammograms (CV) of the sample are presented in Fig. S20c, exhibiting distinct anodic and cathodic peaks for each sample. Notably, the current density obtained over the 10CABB/BWO was found to be three and four times higher than that of V_{Bi-O}BWO and BWO, respectively, indicating a significant catalytic effect of 10CABB/BWO on enhancing the efficient separation of electron-hole pairs. In summary, the photochemical characterization results demonstrate that heterojunction formation between CABB and V_{Bi-O}BWO can accelerate photogenerated electron migration and transport, thereby enhancing the multifunctional photocatalytic conversion for CO_2 reduction.

Based on surface/interfacial catalysis and charge-transfer kinetics analysis, we propose a feasible reaction mechanism for the photocatalytic CO_2 reduction of CABB/V_{Bi-O}BWO (Fig. 7). Considering the abundant multifunctional active sites on the surface of the heterojunction, CO_2 molecules are adsorbed on CABB/V_{Bi-O}BWO via C=O bonds, forming CO_2(C=O)…CABB/V_{Bi-O}BWO surface coordination species, whereas H_2O molecules are adsorbed on the CABB/V_{Bi-O}BWO surface via two coordinated hydrogen-bond interactions to form H_2O (H–O)…CABB/V_{Bi-O}BWO. The activation of reactive molecules is achieved after reaching adsorption equilibrium. Under light irradiation, the CABB/V_{Bi-O}BWO heterogeneous interface provides a short migration pathway for carrier transfer, and the abundant Bi–O defect sites act as electron-capture centres to inhibit the annihilation of photogenerated electrons. The photogenerated electrons are rapidly transferred from CABB to V_{Bi-O}BWO. Subsequently, the photogenerated charges with strong reducibility are effectively captured by CO_2 to form CO_2^- because the conduction band position of CABB/V_{Bi-O}BWO is lower than the electrode potential for CO_2 reduction. Therefore, in the presence of surface four-coordinated water molecules, the photogenerated electrons effectively facilitate the protonation of CO_2 to generate COOH* intermediates, which subsequently undergo continuous reduction to produce CO and CH_4 via protonation. Simultaneously, photogenerated holes are formed in the valence band of CABB in the heterojunction. Photogenerated holes with a strong oxidation capacity have a more positive redox potential than water oxidation. Therefore, H_2O was further oxidised to O_2 by the photogenerated holes. Furthermore, the introduction of Bi–O defects moves the conduction energy of V_{Bi-O}BWO to -1.02 eV, which is more favourable for the photoreduction of CO_2 to CO than the more negative conduction energy of BWO. Finally, the generated CO, CH_4, and O_2 molecules are desorbed from the catalyst surface to realize the photocatalytic reaction cycle.

4. Conclusion

In summary, we successfully fabricated CABB/V_{Bi-O}BWO heterojunction materials as high-efficiency catalysts for CO_2 reduction under visible light irradiation. The CO yield of 10CABB/V_{Bi-O}BWO in the photocatalytic CO_2 reduction reaction was 22 times higher than that of BWO, while the values for CABB (4.2 μmol/g) and BWO (2.2 μmol/g) were much lower. The CO quantum efficiency yield of 10CABB/V_{Bi-O}BWO was up to 0.64%. The mechanism underlying the enhanced activity of CABB/V_{Bi-O}BWO samples was systematically investigated. XAFS, PALS, and DFT experiments demonstrated that a compact heterojunction was formed between the bridged Bi–O vacancies in V_{Bi-O}BWO and CABB through a defect-confinement strategy, in which the exposed Bi atom is considered as the reactive active centre. CO_2 molecules are adsorbed on the exposed Bi sites through the C=O functional group and
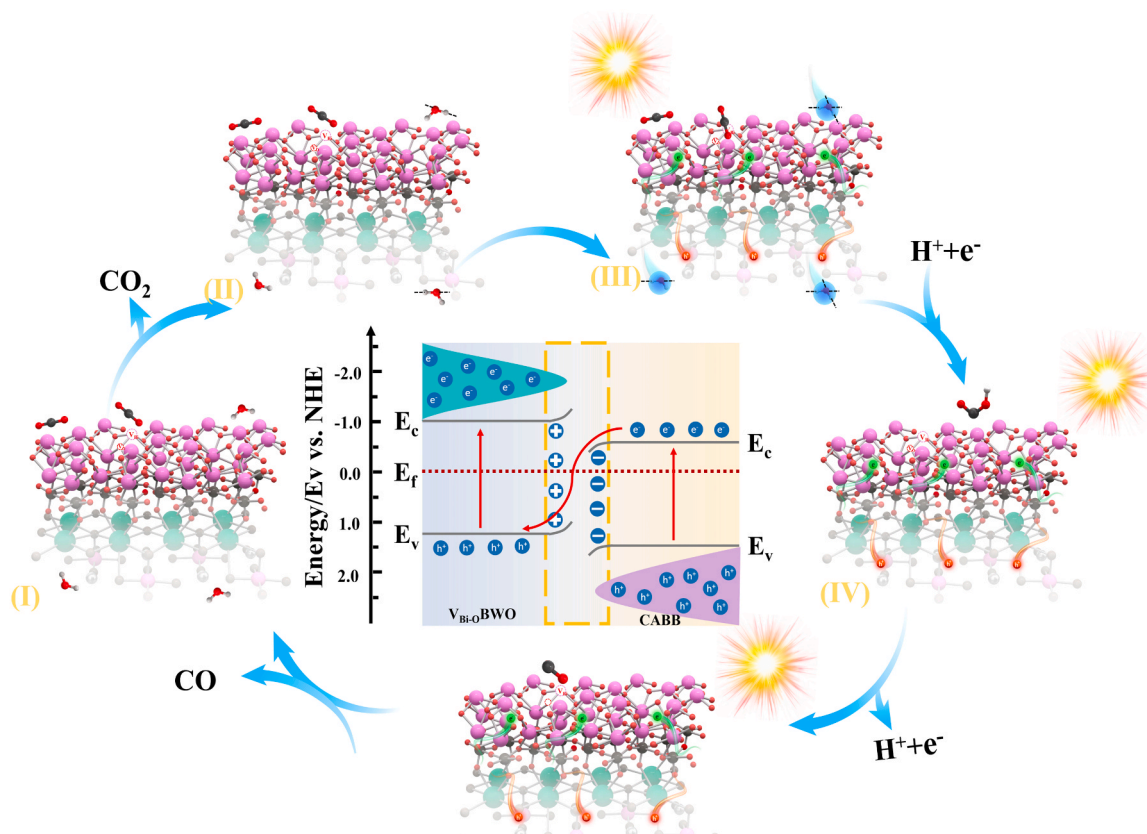

Fig. 7. Schematic diagram of CO_2 photoreduction mechanism on CABB/V_{Bi-O}BWO.

initiate the activation of reactive molecules. CO_2 is protonated to COOH* (in a rate-dependent step) in conjunction with the adsorption of the four-coordinated H_2O molecules on the surface and the photo-generated electrons. In the photocatalytic CO_2 reduction pathway, CABB/V$_{Bi-O}$BWO exhibits the lowest COOH* formation energy barrier, which is beneficial for accelerating the transition of adsorbed COOH* to CO* by regulating the rate-limiting step. Simultaneously, the Bi–O vacancies in CABB/V$_{Bi-O}$BWO promote interfacial strengthening, which effectively enhances the rapid migration and separation of photo-generated charges from CABB to V$_{Bi-O}$BWO (as evidenced by in situ XPS, femtosecond time-resolved spectroscopy, and KPFM characterisation), thus enhancing the photocatalytic CO_2 reduction performance. Based on the above analysis, a well-grounded mechanism for photocatalytic CO_2 reduction is proposed at the molecular level. This work proposes an effective strategy to regulate interfacial charge transfer by reconstruct-ing the heterojunction surface states through defects. Insights into the interaction between the reactive molecules and heterojunction materials at the molecular level were obtained by comprehensive experimental and theoretical analyses.

CRediT authorship contribution statement

Hongbing Ji: Supervision, Funding acquisition, Conceptualization. **Yongming Luo:** Supervision, Funding acquisition, Conceptualization. **Peng Hu:** Validation. **Xilun Wang:** Validation, Methodology. **Hao Wang:** Methodology, Investigation, Data curation. **Ting Liu:** Software, Resources. **Kai-hang Ye:** Methodology. **Bo Weng:** Methodology.

Declaration of Competing Interest

The authors declare that they have no known competing financial interests or personal relationships that could have appeared to influence the work reported in this paper.

Data availability

Data will be made available on request.

Acknowledgements

Appendix A. Supporting information

Supplementary data associated with this article can be found in the online version at doi:10.1016/j.apcatb.2024.123956.

References

[1] Y.Y. Li, Z.S. Liu, Z.Q. Rao, F. Yu, W.T. Bao, Y. Tang, H.H. Zhao, J. Zhang, Z. J. Wang, J.B. Li, Z.A. Huang, Y. Zhou, Y.S. Li, B. Dai, Experimental and theoretical insights into an enhanced CO_2 methanation mechanism over a Ru-based catalyst, Appl. Catal. B Environ. 319 (2022) 121903, https://doi.org/10.1016/j.apcatb.2022.121903.

[2] B. Han, X.W. Ou, Z.Q. Deng, Y. Song, C. Tian, H. Deng, Y.J. Xu, Z. Lin, Nickel metal–organic framework monolayers for photoreduction of diluted CO_2: metal-node-dependent activity and selectivity, Angew. Chem. Int. Ed. 57 (2018) 16811–16815, https://doi.org/10.1002/anie.201811545.

[3] J.C. Zhu, W.W. Shao, X.D. Li, X.C. Jiao, J.F. Zhu, Y.F. Sun, Y. Xie, Asymmetric triple-atom sites confined in ternary oxide enabling selective CO_2 photothermal

reduction to acetate, J. Am. Chem. Soc. 143 (2021) 18233–18241, https://doi.org/10.1021/jacs.1c08033.

[4] A. Wagner, C.D. Sahm, E. Reisner, Towards molecular understanding of local chemical environment effects in electro-and photocatalytic CO_2 reduction, Nat. Catal. 3 (2020) 775–786, https://doi.org/10.1038/s41929-020-00512-x.

[5] M. Bonchio, J. Bonin, O. Ishitani, T.B. Lu, T. Morikawa, A.J. Morris, E. Reisner, D. Sarkar, F.M. Toma, M. Robert, Best practices for experiments and reporting in photocatalytic CO_2 reduction, Nat. Catal. 6 (2023) 657–665, https://doi.org/10.1038/s41929-023-00992-7.

[6] X. Chi, Z.A. Lan, Q. Chen, X.R. Zhang, X. Chen, G.G. Zhang, X.C. Wang, Electronic transmission channels promoting charge separation of conjugated polymers for photocatalytic CO_2 reduction with controllable selectivity, Angew. Chem. Int. Ed. 62 (2023) e202303785, https://doi.org/10.1002/anie.202303785.

[7] F.Y. Xu, K. Meng, B.C. Zhu, H.B. Liu, J.S. Xu, J.G. Yu, Graphdiyne: a new photocatalytic CO_2 reduction cocatalyst, Adv. Funct. Mater. 29 (2019) 1904256, https://doi.org/10.1002/adfm.201904256.

[8] C. Lim, H.R. An, S. Ha, S. Myeong, C.G. Min, H.J. Chung, B. Son, C.Y. Kim, J.I. Park, H. Kim, H.U. Lee, Y.S. Lee, Highly visible-light-responsive nanoporous nitrogen-doped TiO_2 (N-TiO_2) photocatalysts produced by underwater plasma technology for environmental and biomedical applications, Appl. Surf. Sci. 638 (2023) 158123, https://doi.org/10.1016/j.apsusc.2023.158123.

[9] Y.J. Ma, X.X. Yi, S.L. Wang, T. Li, B. Tan, C.C. Chen, T. Majima, E.R. Waclawik, H. Y. Zhu, J.Y. Wang, Selective photocatalytic CO_2 reduction in aerobic environment by microporous Pd-porphyrin-based polymers coated hollow TiO_2, Nat. Commun. 13 (2022) 1400, https://doi.org/10.1038/s41467-022-29102-0.

[10] T. Wang, L. Chen, C. Chen, M.T. Huang, Y.J. Huang, S.J. Liu, B.X. Li, Engineering catalytic interfaces in $Cu^{δ+}$/CeO_2-TiO_2 photocatalysts for synergistically boosting CO_2 reduction to ethylene, ACS Nano 16 (2022) 2306–2318, https://doi.org/10.1021/acsnano.1c08505.

[11] F.Y. Xu, J.J. Zhang, B.C. Zhu, J.G. Yu, J.S. Xu, $CuInS_2$ sensitized TiO_2 hybrid nanofibers for improved photocatalytic CO_2 reduction, Appl. Catal. B-Environ. 230 (2018) 194–202, https://doi.org/10.1016/j.apcatb.2018.02.042.

[12] D. Montalvo, G. Corro, F. Bañuelos, O. Olivares-Xometl, P. Arellanes, U. Pal, Selective alcohols production through CO_2 photoreduction using Co_3O_4/TiO_2 photocatalyst exploiting synergetic interactions between Ti^{3+}, Co^{2+} and Co^{3+}, Appl. Catal. B-Environ. 330 (2023) 122652 https://doi.org/10.1016/j.apcatb.2023.122652.

[13] H.W. Huang, C. Zhou, X.C. Jiao, H.F. Yuan, J.W. Zhao, C.Q. He, J. Hofkens, M.B. J. Roeffaers, J.L. Long, J.A. Steele, Subsurface defect engineering in single-unit-cell Bi_2WO_6 monolayers boosts solar-driven photocatalytic performance, ACS Catal. 10 (2020) 1439–1443, https://doi.org/10.1021/acscatal.9b04789.

[14] S.J. Wu, J.G. Sun, Q. Li, Z.D. Hood, S.Z. Yang, T.M. Su, R. Peng, Z.L. Wu, W.W. Sun, P.R.C. Kent, B. Jiang, M.F. Chisholm, Effects of surface terminations of 2D Bi_2WO_6 on photocatalytic hydrogen evolution from water splitting, ACS Appl. Mater. Interfaces 12 (2020) 20067–20074, https://doi.org/10.1021/acsami.0c01802.

[15] L.B. Xiao, R.B. Lin, J. Wang, C. Cui, J.Y. Wang, Z.Q. Li, A novel hollow-hierarchical structured Bi_2WO_6 with enhanced photocatalytic activity for CO_2 photoreduction, J. Colloid Interface Sci. 523 (2018) 151–158, https://doi.org/10.1016/j.jcis.2018.03.064.

[16] Y.P. Liu, D.Y. Shen, Q. Zhang, Y. Lin, F. Peng, Enhanced photocatalytic CO_2 reduction in H_2O vapor by atomically thin Bi_2WO_6 nanosheets with hydrophobic and nonpolar surface, Appl. Catal. B-Environ. 283 (2021) 119630, https://doi.org/10.1016/j.apcatb.2020.119630.

[17] R. Liu, Y.Z. Shi, L.H. Lin, Z.W. Wang, C. Liu, J.H. Bi, Y.D. Hou, S. Lin, L. Wu, Surface lewis acid sites and oxygen vacancies of Bi_2WO_6 synergistically promoted photocatalytic degradation of levofloxacin, Appl. Surf. Sci. 605 (2022) 154822, https://doi.org/10.1016/j.apsusc.2022.154822.

[18] W.C. Huo, X.A. Dong, J.Y. Li, M. Liu, X.Y. Liu, Y.X. Zhang, F. Dong, Synthesis of Bi_2WO_6 with gradient oxygen vacancies for highly photocatalytic NO oxidation and mechanism study, Chem. Eng. J. 361 (2019) 129–138, https://doi.org/10.1016/j.cej.2018.12.071.

[19] J. Xiong, J. Di, J.X. Xia, W.S. Zhu, H.M. Li, Surface defect engineering in 2D nanomaterials for photocatalysis, Adv. Funct. Mater. 28 (2018) 1801983, https://doi.org/10.1002/adfm.201801983.

[20] S.Q. Zhang, X.S. Yi, G.H. Hu, M.X. Chen, H. Shen, B. Li, L.X. Yang, W.L. Dai, J. P. Zou, S.L. Luo, Configuration regulation of active sites by accurate doping inducing self-adapting defect for enhanced photocatalytic applications: a review, Coord. Chem. Rev. 478 (2023) 214970, https://doi.org/10.1016/j.ccr.2022.214970.

[21] Q. Yao, Z.Y. Yu, L.G. Li, X.Q. Huang, Strain and surface engineering of multicomponent metallic nanomaterials with unconventional phases, Chem. Rev. 123 (2023) 9676–9717, https://doi.org/10.1021/acs.chemrev.3c00252.

[22] H.P. Zhou, D.Y. Zhang, H.C. Xie, Y. Liu, C.X. Meng, P.F. Zhang, F.T. Fan, R.G. Li, C. Li, Modulating oxygen vacancies in lead chromate for photoelectrocatalytic water splitting, Adv. Mater. 35 (2023) 2300914, https://doi.org/10.1002/adma.202300914.

[23] G.B. Wen, B.H. Ren, Y. Zheng, M. Li, C. Silva, S.Q. Song, Z. Zhang, H.Z. Dou, L. Zhao, D. Luo, A.P. Yu, Z.W. Chen, Engineering electrochemical surface for efficient carbon dioxide upgrade, Adv. Energy Mater. 12 (2022) 2103289, https://doi.org/10.1002/aenm.202103289.

[24] M.D. Zhai, C. Chen, M. Cheng, Advancing lead-free $Cs_2AgBiBr_6$ perovskite solar cells: challenges and strategies, Sol. Energy 253 (2023) 563–583, https://doi.org/10.1016/j.solener.2023.02.027.

[25] M.T. Sirtl, R. Hooijer, M. Armer, F.G. Ebadi, M. Mohammadi, C. Maheu, A. Weis, B. T.V. Gorkom, S. Häringer, R.A.J. Janssen, T. Mayer, V. Dyakonov, W. Tress, T. Bein, 2D/3D hybrid $Cs_2AgBiBr_6$ double perovskite solar cells: improved energy

level alignment for higher contact-selectivity and large open circuit voltage, Adv. Energy Mater. 12 (2022) 2103215, https://doi.org/10.1002/aenm.202103215.

[26] Y.Y. Wang, H.L. Huang, Z.Z. Zhang, C. Wang, Y.Y. Yang, Q. Li, D.S. Xu, Lead-free perovskite $Cs_2AgBiBr_6$@g-C_3N_4 Z-scheme system for improving CH_4 production in photocatalytic CO_2 reduction, Appl. Catal. B Environ. 282 (2021) 119570, https://doi.org/10.1016/j.apcatb.2020.119570.

[27] T. Wang, D.T. Yue, X. Li, Y.X. Zhao, Lead-free double perovskite $Cs_2AgBiBr_6$/RGO composite for efficient visible light photocatalytic H_2 evolution, Appl. Catal. B-Environ. 268 (2020) 118399, https://doi.org/10.1016/j.apcatb.2019.118399.

[28] Y.G. Zhou, Y.F. Zhang, M.S. Lin, J.L. Long, Z.Z. Zhang, H.X. Lin, J.C.S. Wu, X. X. Wang, Monolayered Bi_2WO_6 nanosheets mimicking heterojunction interface with open surfaces for photocatalysis, Nat. Commun. 6 (2015) 8340, https://doi.org/10.1038/ncomms9340.

[29] L. Zhou, Y.F. Xu, B.X. Chen, D.B. Kuang, C.Y. Su, Synthesis and photocatalytic application of stable lead-free $Cs_2AgBiBr_6$ perovskite nanocrystals, Small 14 (2018) 1703762, https://doi.org/10.1002/smll.201703762.

[30] J.D. Hu, D.Y. Chen, Z. Mo, N.J. Li, Q.F. Xu, H. Li, J.H. He, H. Xu, J.M. Lu, Z-scheme 2D/2D heterojunction of black phosphorus/monolayer Bi_2WO_6 nanosheets with enhanced photocatalytic activities, Angew. Chem. Int. Ed. 58 (2019) 2073–2077, https://doi.org/10.1002/anie.201813417.

[31] P. Pistor, M. Meyns, M. Guc, H.C. Wang, M.A.L. Margues, X. Alcobé, A. Cabot, V. Izquierdo-Roca, Advanced raman spectroscopy of $Cs_2AgBiBr_6$ double perovskites and identification of $Cs_3Bi_2Br_9$ secondary phases, Scr. Mater. 184 (2020) 24–29, https://doi.org/10.1016/j.scriptamat.2020.03.040.

[32] J.A. Steele, P. Puech, M. Keshavarz, R.X. Yang, S. Banerjee, E. Debroye, C.W. Kim, H.F. Yuan, N.H. Heo, J. Vanacken, A. Walsh, J. Hofkens, M.B.J. Roeffaers, Giant electron−phonon coupling and deep conduction band resonance in metal halide double perovskite, ACS Nano 12 (2018) 8081–8090, https://doi.org/10.1021/acsnano.8b02936.

[33] Y.K. Huang, S.F. Kang, Y. Yang, H.F. Qin, Z.J. Ni, S.J. Yang, X. Li, Facile synthesis of Bi/Bi_2WO_6 nanocomposite with enhanced photocatalytic activity under visible light, Appl. Catal. B-Environ. 196 (2016) 89–99, https://doi.org/10.1016/j.apcatb.2016.05.022.

[34] J. Di, C. Chen, C. Zhu, M.X. Ji, J.X. Xia, C. Yan, W. Hao, S.Z. Li, H.M. Li, Z. Liu, Bismuth vacancy mediated single unit cell Bi_2WO_6 nanosheets for boosting photocatalytic oxygen evolution, Appl. Catal. B-Environ. 238 (2018) 119–125, https://doi.org/10.1016/j.apcatb.2018.06.066.

[35] H.B. Fu, L.W. Zhang, W.Q. Yao, Y.F. Zhu, Photocatalytic properties of nanosized Bi_2WO_6 catalysts synthesized via a hydrothermal process, Appl. Catal. B-Environ. 66 (2006) 100–110, https://doi.org/10.1016/j.apcatb.2006.02.022.

[36] X.L. Zu, Y. Zhao, X.D. Li, R.H. Chen, W.W. Shao, Z.Q. Wang, J. Hu, J.F. Zhu, Y. Pan, Y.F. Sun, Y. Xie, Ultrastable and efficient visible-light-driven CO_2 reduction triggered by regenerative oxygen-vacancies in $Bi_2O_2CO_3$ Nanosheets, Angew. Chem. Int. Ed. 60 (2021) 13840–13846, https://doi.org/10.1002/anie.202101894.

[37] D.X. Ji, L. Fan, L. Tao, Y.J. Sun, M.G. Li, G.R. Yang, T.Q. Tran, S. Ramakrishna, S. J. Guo, The kirkendall effect for engineering oxygen vacancy of hollow Co_3O_4 nanoparticles toward high-performance portable zinc–air batteries, Angew. Chem. Int. Ed. 58 (2019) 13840–13844, https://doi.org/10.1002/anie.201908736.

[38] M. Kim, B. Lee, H. Ju, J.Y. Kim, J. Kim, S.W. Lee, Oxygen-vacancy-introduced $BaSnO_{3−δ}$ photoanodes with tunable band structures for efficient solar-driven water splitting, Adv. Mater. 31 (2019) 1903316, https://doi.org/10.1002/adma.201903316.

[39] L. Zhang, C. Yang, K.L. Lv, Y.C. Lu, Q. Li, X.F. Wu, Y.H. Li, X.F. Li, J.J. Fan, M. Li, SPR effect of bismuth enhanced visible photoreactivity of Bi_2WO_6 for NO abatement, Chin. J. Catal. 40 (2019) 755–764, https://doi.org/10.1016/S1872-2067(19)63320-6.

[40] Y. Jiang, H.Y. Chen, J.Y. Li, J.F. Liao, H.H. Zhang, X.D. Wang, D.B. Kuang, Z-scheme 2D/2D heterojunction of $CsPbBr_3/Bi_2WO_6$ for improved photocatalytic CO_2 reduction, Adv. Funct. Mater. 30 (2020) 2004293, https://doi.org/10.1002/adfm.202004293.

[41] L. Liu, J.Q. Liu, K.L. Sun, J. Wan, F. Fu, J. Fan, Novel phosphorus-doped Bi_2WO_6 monolayer with oxygen vacancies for superior photocatalytic water detoxication and nitrogen fixation performance, Chem. Eng. J. 411 (2021) 128629, https://doi.org/10.1016/j.cej.2021.128629.

[42] S.W. Cao, B.J. Shen, T. Tong, J.W. Fu, J.G. Yu, 2D/2D heterojunction of ultrathin MXene/Bi_2WO_6 nanosheets for improved photocatalytic CO_2 reduction, Adv. Funct. Mater. 28 (2018) 1800136, https://doi.org/10.1002/adfm.201800136.

[43] Q.Q. Fan, S.Y. Wei, J.Z. Ma, W.B. Zhang, L. Wen, Water-driven boost in the visible light photocatalytic performance of $Cs_2AgBiBr_6$ double perovskite nanocrystals, J. Mater. Chem. A 10 (2022) 14923–14932, https://doi.org/10.1039/D2TA03217A.

[44] F.X. Ji, Y.Q. Huang, F. Wang, L. Kobera, F.Y. Xie, J. Klarbring, S. Abbrent, J. Brus, C.Y. Yin, S.I. Simak, I. Abrikosov, I. Buyanova, W. Chen, F. Gao, Near-infrared light-responsive Cu-doped $Cs_2AgBiBr_6$, Adv. Funct. Mater. 30 (2020) 2005521, https://doi.org/10.1002/adfm.202005521.

[45] H.W. Huang, R.R. Cao, S.X. Yu, K. Xu, W.C. Hao, Y.G. Wang, F. Dong, T. Zhang, Y. H. Zhang, Single-unit-cell layer established Bi_2WO_6 3D hierarchical architectures: efficient adsorption, photocatalysis and dye-sensitized photoelectrochemical performance, Appl. Catal. B-Environ. 2019 (2017) 526–537, https://doi.org/10.1016/j.apcatb.2017.07.084.

[46] X. Cao, Z. Chen, R. Lin, W.C. Cheong, S.J. Liu, J. Zhang, Q. Peng, C. Chen, T. Han, X.J. Tong, Y. Wang, R.G. Shen, W. Zhu, D.S. Wang, Y.D. Li, A photochromic composite with enhanced carrier separation for the photocatalytic activation of benzylic C–H bonds in toluene, Nat. Catal. 1 (2018) 704–710, https://doi.org/10.1038/s41929-018-0128-z.

[47] X.J. Ren, J.W. Yao, L. Cai, J.B. Li, X.Z. Cao, Y.F. Zhang, B.Y. Wang, Y. Wei, Band gap engineering of BiOI via oxygen vacancies induced by graphene for improved photocatalysis, New J. Chem. 43 (2019) 1523, https://doi.org/10.1039/C8NJ05538F.

[48] Z.Q. Wang, L.L. Zhang, X. Zhang, C. Hu, L. Wang, B.Y. Shi, X.Z. Cao, Enhanced photocatalytic destruction of pollutants by surface W vacancies in V_W-Bi_2WO_6 under visible light, J. Colloid Interface Sci. 576 (2020) 385–393, https://doi.org/10.1016/j.jcis.2020.05.047.

[49] Y.H. Wang, S.S. Zheng, W.M. Yang, R.Y. Zhou, Q.F. He, P. Radjenovic, J.C. Dong, S. N. Li, Z.L. Yang, G. Attard, F. Pan, Z.Q. Tian, J.F. Li, In situ raman spectroscopy reveals the structure and dissociation of interfacial water, Nature 600 (2021) 81–85, https://doi.org/10.1038/s41586-021-04068-z.

[50] M.H. Zhang, Y.Y. Mao, X.L. Bao, G.Y. Zhai, D.F. Xiao, D. Liu, P. Wang, H.F. Cheng, Y.Y. Liu, Z.K. Zheng, Y. Dai, Y.C. Fan, Z.Y. Wang, B.B. Huang, Coupling benzylamine oxidation with CO_2 photoconversion to ethanol over a black phosphorus and bismuth tungstate S-scheme, Angew. Chem. Int. Ed. 135 (2023) e202302919, https://doi.org/10.1002/ange.202302919.

[51] Y.H. Wang, J.C. Hu, T. Ge, F. Chen, Y. Lu, R.H. Chen, H.J. Zhang, B.J. Ye, S. Y. Wang, Y.H. Zhang, T.Y. Ma, H.W. Huang, Gradient Cationic Vacancies Enabling Inner-To-Outer Tandem Homojunctions: strong Local Internal Electric Field and Reformed Basic Sites Boosting CO_2 Photoreduction, Adv. Mater. 35 (2023) 2302538, https://doi.org/10.1002/adma.202302538.

[52] J. Li, W.F. Pan, Q.Y. Liu, Z.Q. Chen, Z.J. Chen, X.Z. Feng, H. Chen, Interfacial engineering of $Bi_{19}Br_3S_{27}$ nanowires promotes metallic photocatalytic CO_2 reduction activity under near-infrared light irradiation, J. Am. Chem. Soc. 143 (2021) 6551–6559, https://doi.org/10.1021/jacs.1c01109.

[53] S. Karmakar, S. Barman, F.A. Rahimi, T.K. Maji, Covalent grafting of molecular photosensitizer and catalyst on MOF-808: effect of pore confinement toward visible light-driven CO_2 reduction in water, Energy Environ. Sci. 14 (2021) 2429–2440, https://doi.org/10.1039/D0EE03643A.

[54] X.D. Li, Y.F. Sun, J.Q. Xu, Y.J. Shao, J. Wu, X. Xu, Y. Pan, H.X. Ju, J.F. Zhu, Y. Xie, Selective visible-light-driven photocatalytic CO_2 reduction to CH_4 mediated by atomically thin $CuIn_5S_8$ layers, Nat. Energy 4 (2019) 690–699, https://doi.org/10.1038/s41560-019-0431-1.

[55] K.H. Ye, H.B. Li, D. Huang, S. Xiao, W.T. Qiu, M.Y. Li, Y.W. Hu, W.J. Mai, H.B. Ji, S. H. Yang, Enhancing photoelectrochemical water splitting by combining work function tuning and heterojunction engineering, Nat. Commun. 10 (2019) 3687, https://doi.org/10.1038/s41467-019-11586-y.

[56] J. Liu, Y. Liu, N.Y. Liu, Y.Z. Han, X. Zhang, H. Huang, Y. Lifshitz, S.T. Lee, J. Zhong, Z.H. Kang, Metal-free efficient photocatalyst for stable visible water splitting via a two-electron pathway, Science 347 (2015) 970–974, https://doi.org/10.1126/science.aaa3145.